Measured atmospheric $^{36}Ar/^{38}Ar$, $^{20}Ne/^{22}Ne$, $^{36}Ar/^{22}Ne$ noble gas isotope and bulk K/U ratios constrain the early evolution of Venus and Earth

H. Lammer[a], M. Leitzinger[a,b], M. Scherf[a], P. Odert[a,b], C. Burger[c], D. Kubyshkina[a], C. Johnstone[c], T. Maindl[c], C. M. Schäfer[d], M. Güdel[c], N. Tosi[e,f], A. Nikolaou[e,f], E. Marcq[g], N. V. Erkaev[h,i], L. Noack[j], K. G. Kislyakova[c,a], L. Fossati[a], E. Pilat-Lohinger[c], F. Ragossnig[c], E. A. Dorfi[c]

[a]*Space Research Institute, Austrian Academy of Sciences, Graz, Austria*
[b]*Institute of Physics/IGAM, University of Graz, Austria*
[c]*Department of Astrophysics, University of Vienna, Austria*
[d]*Institute of Astronomy and Astrophysics, University of Tübingen, Germany*
[e]*Institute of Planetary Research, Department of Planetary Physics, DLR, Berlin Germany*
[f]*Department of Astronomy and Astrophysics, Berlin Institute of Technology, Germany*
[g]*LATMOS, Université de Versailles Saint-Quentin-en-Yvelines, Guyancourt, France*
[h]*Institute of Computational Modelling SB RAS, Krasnoyarsk, Russian Federation*
[i]*Siberian Federal University, Krasnoyarsk, Russian Federation*
[j]*Department of Earth Sciences, Freie Universität Berlin, Germany*

Abstract

The atmospheric noble gas isotope and elemental bulk ratios on Venus and Earth provide important information on their origin and evolution. If the protoplanets grew to a certain mass (i.e. > 0.5 M_{Earth}, they could have captured H_2-dominated primordial atmospheres by accreting gas from the circumstellar disk during the formation of the Solar System, which were then quickly lost by hydrodynamic escape after the disk dissipated. In such a case, the EUV-driven hydrodynamic flow of H atoms dragged heavier elements with it at different rates, leading to changes in their initial isotope ratios. For reproducing Earth and Venus present atmospheric $^{36}Ar/^{38}Ar$, $^{20}Ne/^{22}Ne$, $^{36}Ar/^{22}Ne$, isotope and bulk K/U ratios we applied hydrodynamic upper atmosphere escape and Smooth Particle Hydrodynamics (SPH) impact models for the calculation of captured H_2-dominated primordial atmospheres for various protoplanetary masses. We

Email address: helmut.lammer@oeaw.ac.at (H. Lammer)

investigated a wide range of possible EUV evolution tracks of the young Sun and initial atmospheric compositions based on mixtures of captured nebula gas, outgassed and delivered material from ureilite, enstatite and carbonaceaous chondrites. Depending on the disk lifetime of ≈ 3-5 Myr (Bollard et al., 2017; Wang et al., 2017) and the composition of accreted material after disk dispersal, we find from the reproduction of the present atmospheric Ar, Ne, and bulk K/U ratios, that early Earth's evolution can be explained if proto-Earth had accreted masses between ≈ $0.53 - 0.58\ M_{\mathrm{Earth}}$ by the time the nebula gas dissipated. If proto-Earth would have accreted a higher mass during the disk lifetime the present atmospheric Ar and Ne isotope ratios can not be reproduced with our model approach. For masses > $0.75 M_{\mathrm{Earth}}$, Earth would have had a problem to get get rid of its primordial atmosphere. If proto-
Earth accreted ≈ $0.53 - 0.58 M_{\mathrm{Earth}}$ of enstatite-dominated material as suggested by Dauphas (2017) during the disk lifetime, it would have captured a tiny primordial atmosphere that was lost ≈3 Myr after the disk dissipated. In such a case we find that the present-day atmospheric Ar and Ne isotope ratios can be best reproduced if the post-nebula impactors contained ≈ 5% weakly depleted carbonaceous chon- dritic material and ≈95% enstatite chondrites that are strongly depleted in Ar, Ne and moderately volatile elements like potassium. If higher amounts of carbona- ceous chondrites were involved in early Earth's accretion as recently suggested by Schiller et al. (2018), then the Earth's present atmospheric Ar and Ne ratios can only be reproduced if the involved carbonaceous chondritic post-nebula material was also highly depleted in these noble gases and/or had to be partially be delivered as long as the primordial atmosphere was yet escaping. As long as primordial atmo- spheres surround the growing protoplanets the abundance of their volatile elements is
overwritten by their respective captured solar-like atmospheric abundances. Therefore the initial composition of the protoplanets at the disk dispersal time can not be iden- tified by our method. For masses less than $0.5\ M_{\mathrm{Earth}}$ atmospheric escape cannot

explain the present-day ratios, i.e. if Earth grew slower then these ratios have to be explained differently (Marty, 2012). If proto-Venus captured a primordial atmosphere it should have grown to masses of $\approx 0.8 - 1.0\ M_{\mathrm{Venus}}$ during the time until the disk dissipated and if early Venus accreted its main mass during the disk lifetime than the present atmospheric Ar and Ne isotope ratios and the observed K/U ratios on Venus surface can also be reproduced by the escape of a captured primordial atmosphere that is lost within ≤ 100 Myr, if the Sun was born between a weakly and moderately active young G star. New precise re-measurements of atmospheric noble gases are necessary by future Venus missions to better con- strain the material that was involved in the planet's accretion history and possibly also the EUV activity evolution of the young Sun. In addition, measurements of other moderately volatile element and isotope ratios on the surface such as Rb/U, ^{64}Zn/^{66}Zn, and ^{39}K/^{41}K can give an insight on whether Venus accreted slow or fast, i.e. almost to its final mass within the disk lifetime.

1. Introduction

The bulk composition of the silicate part of the Solar System planets has long been linked to chondritic meteorites (e.g. Taylor, 1964; Anders and Grevesse, 1989; Dauphas, 2017; Schiller et al., 2018). Venus and Earth are expected to have formed over several million years by accretion of planetesimals and planetary embryos originating from various heliocentric distances, with the majority coming from a narrow annulus near 1 AU (O'Brien et al., 2006). Ruthenium (Ru) isotope studies related to primitive meteoritic material indicate that the terrestrial planets received the main fraction of their volatiles by accretion of volatile-rich bodies from the outer Solar System during the main stage of their formation and not during the late accretion phase, i.e. the late veneer which comprises the last ≈0.5% (Fischer-Gödde and Kleine, 2017). A more recent study, however, based on Selenium isotopes contrarily suggests that the late veneer

originated from carbonaceous chondrites originating in sthe out Solar System and was volatile rich (Varas-Reus et al., 2019).

The building blocks of the most primitive meteorites formed from thermally processed depleted inner disk material relative to material that formed in the outer regions. These inner and outer regions comprise two distinct reservoirs of planet forming material that were not mixed initially (Budde et al., 2019), i.e. the non-carbonaceous chondritic (NCC) and the carbonaceous chondritic (CC) reservoirs.

Marty (2012) analyzed the noble gases of the present Earth atmosphere and concluded that the ratios of today's atmosphere and concentrations of water, carbon and nitrogen indicate a volatile content equivalent to an ≈98% non-chondritic dry proto-Earth with ≈2% contribution of carbonaceous CI-CM-like (CC) material during the main Earth-forming events. Based on the analysis of $^{36}Ar/^{22}Ne$ isotope data from Earth's atmosphere, rocks related to its interior (Moreira et al., 1998) and well gases (Ballentine et al., 2005) the $^{20}Ne/^{22}Ne$ end member (planetary-A) matches carbonaceous chondrites and not enstatite or ordinary chondrites (Marty, 2012). According to this pioneering study by Marty (2012) the present atmospheric Ar and Ne isotope ratios do not necessarily require isotopic fractionation during hy- drodynamic escape of an early primordial atmosphere (see Fig. 3 in (Marty, 2012)).

More recently, Dauphas (2017) found that elements with distinct affinities for metal can be used to reveal the isotopic nature of early Earth's accreting material through time. Isotope measurements of ^{17}O, ^{48}Ca, ^{50}Ti, ^{54}Cr, ^{64}Ni, ^{92}Mo, ^{100}Ru indicate that the Earth has isotopic compositions that almost match enstatite meteorites (e.g. Javoy et al., 2010; Dauphas et al., 2014; Dauphas and Schauble, 2016). Dauphas (2017) analyzed isotopic signatures of lithophile (O, Ca, Ti, Nd), moderately siderophile (Cr, Ni and Mo) and highly siderophile elements (Ru) from Earth's mantle and found that they record different stages of its accretion. According to this analysis

the best-fitting model of the first 60% of proto-Earth's mass consisted of about ≈ 51 % enstatite chondrites (EC), ≈ 40 % ordinary chondrites (OC) and ≈ 9% carbonaceous chondrites (CC: an average over CI, CO, CV), whereas all of the remaining accreted material consisted mainly of enstatite-like impactors.

A recent study by Schiller et al. (2018) investigated Ca for understanding the secular evolution of the nucleosynthetic composition of the disk material that accreted to growing protoplanets. These authors determined the mass-independent $^{48}Ca/^{44}Ca$ isotope composition of selected Solar System objects, including angrites, eucrites, ureilites, Lunar and Martian meteorites, ordinary and carbonaceous chondrites, and individual very young chondrules from ordinary and carbonaceous chondrites. It was found that the Ca-isotope composition of different planetary bodies in the inner Solar System correlates with their masses. Schiller et al. (2018) suggest that all planetary embryos grew at the same rate, but stopped growing at different times so that smaller bodies ceased their accretion earlier than did larger ones. This unorthodox hypothesis of growth is, however, also supported by numerical simulations (Levison et al., 2015; Morbidelli, 2018).

According to this analysis the inner Solar System chondrules indicate that the $^{48}Ca/^{44}Ca$ composition of early inner disk material evolved from an ureilite-like to a terrestrial composition within ≈1 Myr after the formation of the Sun. From their analysis these authors suggest that the Earth accreted from ≈ 60% ureilite-like (UR) inner disk material and ≈40% mainly CI chondrites from the outer Solar System. It has been argued by Budde et al. (2019) that a mixture of carbonaceous chondritic and non-carbonaceous chondritic material such as ureilites might also achieve some of the isotopic compositions of the terrestrial building blocks.

By comparing the findings of Dauphas (2017) based on lithophile-siderophile isotopic affinities of Earth's accreting material and the recent findings by Schiller et al. (2018) based on their Ca-isotope composition data of different planetary bodies

one can see that our understanding of terrestrial planet formation is most likely incomplete. According to Morbidelli (2018) these findings need to be connected with other findings provided by chemical, chronological, isotopical and dynamical constraints.

Although these findings, including that of Marty (2012), might seem to contradict each other, this is not necessarily the case. A variety of different processes such as thermal processing in the primordial atmosphere and atmospheric escape must have had a dramatic impact on the bulk and isotopic compositions of planetary embryos, being possibly a major factor in volatile depletion. For instance, after dissipation of the solar nebula, protoplanets were susceptible to strong volatile loss by either hydrodynamic escape of their accreted primordial hydrogen atmospheres (Erkaev et al., 2015, 2016; Kubyshkina et al., 2018b) or of their magma ocean outgassed primary atmosphere (Odert et al., 2018; Benedikt et al., 2019).

Therefore, impacting planetary embryos that collide with growing protoplanets after the disk evaporated were most likely depleted in volatile elements such as noble gases and/or rock forming elements (Benedikt et al., 2019; Young et al., 2019; Sossi et al., 2019). If these processes played a crucial role in the evolution of the Earth's volatile content, then these studies might be considered as non-contradicting, with the work of Marty (2012) representing present Earth after the early phase of volatile loss and Dauphas (2017), and/or Schiller et al. (2018) or a mixture of both representing proto-Earth.

Recently Wang et al. (2017) constrained the nebula lifetime of the Solar System by meteorite paleomagnetism to be within the age of ≈3.7-3.9 Myr after formation of the Sun. This age agrees with the study by Bollard et al. (2017) who analyzed the 22 youngest chondrules and inferred from lead (Pb) isotopic ages a minimum and maximum lifetime of the active phase of the protoplanetary disk in the Solar System of ≈3.3-4.5 Myr. This time scale of the lifetime of the solar circumstellar disk fits well

within observations of young stellar disk lifetimes that last mainly between 1-10 Myr (Montmerle et al., 2006; Evans et al., 2009; Mamajek, 2009).

If a protoplanet reached a mass $>0.5M_{\mathrm{Earth}}$ before the protoplanetary nebula evaporated it could have captured a small H_2-dominated envelope (e.g. Hayashi, 1981; Ikoma and Genda, 2006; Stökl et al., 2015, 2016). In the case of Earth, there are studies based on measurements of $^{20}Ne/^{22}Ne$ isotope ratios from mantle material indicating that a fraction of noble gases have also been trapped in solar composition from the protoplanetary disk within its interior (e.g. Mizuno et al., 1980; Porcelli et al., 2001; Yokochi and Marty, 2004; Mukhopadhyay, 2012).

This interpretation, however, is still debated. Other researchers argued that these ratios could be reproduced through implantation of solar wind onto accreted meteoritic material (Raquin and Moreira, 2009; Trieloff et al., 2000; Moreira and Kurz, 2013; Moreira and Charnoz, 2016; Péron et al., 2016; Jaupart et al., 2017; Péron et al., 2018). A more recent study measured values up to 13.03±0.04 from deep mantle plumes and determined a $^{20}Ne/^{22}Ne$ ratio for the primordial plume mantle of 13.23±0.22 (Williams and Mukhopadhyay, 2019) which is indistinguishable from the nebular ratio. While these authors suggest this to be a robust evidence for a reservoir of nebular gas preserved in the deep mantle, it might also be explained by afore mentioned solar wind implantation in case that the irradiation of the solar wind onto the accreted material was very short (Moreira and Charnoz, 2016). However, if the assumption by Williams and Mukhopadhyay (2019) is true then i. proto-Earth must have grown to a certain mass that allowed to accrete an H_2-envelope (Sekiya et al., 1980; Sasaki and Nakazawa, 1990; Ikoma and Genda, 2006; Stökl et al., 2016), ii. proto-Earth must have had a magma ocean (Bouhifd and Jephcoat, 2011; Stökl et al., 2016; Lammer et al., 2018) that interacted with the surrounding primordial atmosphere and iii. one needs to account for the present Earth's atmospheric $^{20}Ne/^{22}Ne$ and $^{36}Ar/^{22}Ne$ isotope ratios which can also be explained without any hydrodynamic

escape of an early primordial atmosphere (Marty, 2012).

Furthermore, under these extreme conditions, significant amounts of major rock-forming elements (e.g., K, Si, Mg, Fe, Ca, Al, Na, S, P, Cl, F) and other moderately volatile elements like Rb or Zn with condensation temperatures of ≤1000 K (Lodders et al., 2009) populate the hot accretionary atmospheres to significant amounts (Schaefer and Fegley, 2010; Fegley et al., 2016) and can therefore be lost via atmospheric escape as previously suggested for the observed depletion of K relative to U (see Fig. 1) (Albarède and Blichert-Toft, 2007). In addition, most solubility data of noble gases in melts support their incompatibility (Carroll et al., 1994), therefore one can assume that most Ar and Ne isotopes have also been outgassed from the magma oceans that formed below the H_2-envelopes (Sekiya et al., 1980; Sasaki and Nakazawa, 1990; Bouhifd and Jephcoat, 2011). In this case isotopes with solar-abundance that were embedded in the nebular gas mixed with those that had the composition and corresponding ratios of the growing protoplanet.

The trace element potassium (K) is important since its radioactive heat producing isotope ^{40}K contributes to the thermal evolution of planetary interiors and global processes such as the generation of long-lived magnetic dynamos (Turcotte and Schubert, 2002; Murthy et al., 2003; Nimmo, 2007). Different amounts of ^{40}K can therefore have severe implications for the habitability of a planet, since a different heat budget in a planet's interior might effect the onset and duration of a dynamo and of tectonic activity. Venus, for instance, does presently not show either, whereas Earth does. This might be reflected in the K/U ratio and K abundance (Jellinek and Jackson, 2015) (Fig. 1). As shown in Fig. 1 a significant depletion of K can be seen in the K/U ratio of each planet (e.g. ≈13800 for the bulk silicate Earth (BSE) (Arevalo et al., 2009; Lodders et al., 2009), and ≥7000 on Venus' surface (Davis et al., 2005)), with respect to a K/U abundance ratio of ≈64650 in the solar photosphere (Lodders et al., 2009) and 68928 in unprocessed chondrites (Lodders et al., 2009). This divergence from the initial ratio

indicates that K was efficiently depleted in early planetary evolution compared to the heavier U. Potassium is moderately volatile with a condensation temperature of ≈1000 K (Lodders, 2003), while U is highly refractory (≈1610 K (Lodders, 2003)). Both elements are lithophile, i.e. tend to go into the crust and mantle during differentiation, and geochemically incompatible so that they do not fractionate via collisional erosion (O'Neill and Palme, 2008).

Depending on the protoplanetary mass and the possible differences in the extreme ultraviolet (EUV) flux evolution of the young Sun (Tu et al., 2015), captured H_2-envelopes of low mass protoplanets can be lost due to hydrodynamic escape (Lammer et al., 2014; Tu et al., 2015; Johnstone et al., 2015) that drags and fractionates heavier species (Zahnle and Kasting, 1986; Hunten et al., 1987; Odert et al., 2018). The detailed conditions under which this escape takes place led to the diverse isotope and elemental ratios observed in Solar System planets (Donahue, 1986; Pepin, 2006; Davis et al., 2005; Odert et al., 2018).

One may wonder why other isotopes of masses similar to Ne and Ar or lower, especially nitrogen (i.e. ^{14}N, ^{15}N), do not show a strong enrichment - such as in the Martian atmosphere (e.g. Füri and Marty, 2015) - of the heavier one in Earth's and Venus' atmospheres. Nitrogen was delivered in the form of NH_3 clathrate, amino acids and other organic compounds during the planetary accretion phase, by planetesimals that originated beyond the ice line (Lammer et al. (2018) and references therein). The growing protoplanets developed magma oceans, and thus hot and extreme surface conditions, during the first tens to hundred Myr (Wordsworth, 2016; Lammer et al., 2018, 2019). At such extreme conditions abiotic atmospheric-surface weathering processes were capable of transferring atmospheric nitrogen efficiently into the surface and mantle via direct dissolution of reduced nitrogen in the early magma ocean(s) during and just after accretion (Wordsworth, 2016). Additionally, atmospheric N_2 also underwent fixation via weathering caused by lightning, shock heating via impactors,

and energetic particles. Because of this, one can expect that volatiles like N_2, including their isotopes, were more or less absent compared to Ar, Ne isotopes or elements like K, Na, Mg, etc. in the early protoplanetary atmospheres (Wordsworth, 2016; Lammer et al., 2018, 2019). Therefore, its isotopes (^{14}N, ^{15}N) on Earth and Venus did not experience isotope fractionation by atmospheric escape, avoiding ^{15}N-enrichment. In case of the Earth, as soon as the planet's crust and upper mantle oxidized ≈4 Gyr ago (a time when no H_2/He was present anymore), N_2 was released efficiently via secondary outgassing by volcanoes (Mikhail and Sverjensky, 2014; Lammer et al., 2018, 2019). The enrichment of ^{15}N isotopes in today's martian atmosphere is generally thought to indicate that the less massive Mars lost its outgassed nitrogen inventory to space by escape processes that did not work on Earth and Venus (i.e. photochemical escape, sputtering; e.g. Fox and Hać (1997); Füri and Marty (2015); Lammer et al. (2018, 2019)). Heavier atmospheric noble gas isotopes of Kr and Xe are too massive to be efficiently fractionated by atmospheric drag of escaping H atoms. However, heavy Xe isotopes in the Earth's mantle and atmospheric Xe in Earth and Mars are isotopically fractionated (see e.g. Ozima and Podosek (1983); Hébrard and Marty (2014); Conrad et al. (2016); Cassata (2017); Avice et al. (2018). On Earth, Xe isotopes may have experienced photochemical fractionation during the Archean period in organic hazes (Hébrard and Marty, 2014; Avice et al., 2018). Another Xe fraction should then have escaped to space via ionized polar outflow in a hydrogen-rich upper atmosphere, which originated from dissociation of CH_4 (Zahnle, 2015; Zahnle et al., 2019; Catling and Kasting, 2017; Avice et al., 2018). As mentioned above, Mars, because of its low mass, could not capture a relevant H_2/He-envelope; therefore, non-thermal escape processes (i.e., ion pick up, sputtering, dissociative recombination) were involved in its noble gas, isotopic and elemental fractionation e.g. Jakosky et al. (1994); Hutchins and Jakosky (1996); Jakosky et al. (2017).

In the past, various researchers attempted to reproduce the present day atmospheric

$^{36}Ar/^{38}Ar$, and $^{20}Ne/^{22}Ne$ noble gas isotope ratios on Venus and Earth (e.g. Pepin, 1991, 1997; Gillmann et al., 2009). These studies, however, applied simple atmo- spheric escape models and arbitrary assumptions about the early solar radiation and plasma environments, and on the initial hydrogen amount of their early atmospheres. Moreover, the possible escape of the radioactive heat producing element K from a primordial atmosphere was never modeled at all. Since measurements of the K/U ratio are also available for Venus (Surkov et al., 1976; Abdrakhimov and Basilevsky, 2002; Basilevsky, 1997) we aim for the first time at reproducing the above mentioned atmo- spheric Ar, Ne noble gas and bulk K/U ratios of both planets simultaneously within a reasonable set of initial conditions based on the hypotheses of Dauphas (2017) and Schiller et al. (2018) implemented by a sequence of models described below:

- a hydrodynamic upper atmosphere model for the calculation of the captured H_2-envelope that remains after the boil-off phase during disk dispersal for various protoplanetary masses (Kubyshkina et al., 2018b,a);
- an upper atmosphere model for the EUV-driven hydrodynamic H atom escape, including heavy isotopes/element dragging (Odert et al., 2018);
- a model for the estimation of magma ocean depths;
- Smooth Particle Hydrodynamics (SPH) model impact simulations for estimating average atmospheric mass losses caused by Moon- and Mars-like impactors with different impact angles and velocities (Burger et al., 2018).

In addition our approach also considers:

- various different evolution scenarios of the young Sun's EUV flux that are constrained by an activity-rotation relation of young solar-like stars (Tu et al., 2015);
- an initial atmospheric composition based on a mixture of captured nebular gas and outgassing from the magma ocean based on different compositions of the protoplanet;

- mass additions via Moon- and Mars-like impactors and the related gravity change up to the final planet and its effect on the photospheric radius and the corresponding escape rates;
- modification of isotope ratios by different reasonable compositions for the impacting material.

By reproducing the measured atmospheric $^{36}Ar/^{38}Ar$, $^{20}Ne/^{22}Ne$ and the bulk K/U ratios on Venus and Earth via atmospheric escape simulations we are able to constrain the growth rate of both planets in the presence of the solar nebular as well as a certain range for the EUV flux evolution of the young Sun. To determine the **upper limit of the** protoplanetary masses of Venus and Earth at the time when the disk evaporated together with a range of solar EUV flux evolution scenarios that can reproduce present day measurements within their error bars we perform a χ^2 parameter study over within reasonable uncertainties. For successful reproduction attempts we also simulate additional isotopical and elemental ratios such as $^{36}Ar/^{22}Ne$, $^{39}K/^{41}K$, $^{64}Zn/^{66}Zn$ and Rb/U. Sect. 2 describes the models, including their input parameters and the used data. In Sect. 3 and 4 we present and discuss the results and the implications of our study for terrestrial planet formation and habitability. Sect. 5 concludes the work.

2. Model description

2.1. Initially accumulated primordial atmospheres

In gaseous accretion, a growing protoplanet gravitationally attracts nebular gas to form an H_2-dominated solar-composition atmosphere. The phase at the end of the disk lifetime is known as "boil-off" and can last from 0.1 up to a few Myr (Lammer et al., 2016; Owen and Wu, 2016). During this phase, the protoplanet's photospheric radius r_{ph} of the H_2-dominated envelope decreases due to the strong thermal loss of hydrogen. During this phase characterized by high thermal atmospheric escape, r_{ph} shrinks rapidly until the escape flux become first equal to and then smaller than the maximum possible

EUV-driven escape flux F_{EUV} (Fossati et al., 2017). As a consequence, the atmosphere flows upwards, even without additional external energy inputs, such as the stellar EUV flux. In this case, the stellar EUV flux is not the main driver of the atmospheric escape (Lammer et al., 2016; Owen and Wu, 2016; Fossati et al., 2017). The extent of the remaining gravitationally-bound H_2-envelope of the protoplanet after this short phase depends strongly on the protoplanetary mass M_{pl} and equilibrium temperature at the orbit location.

We estimate the range of equilibrium temperatures after the origin of the Sun by using stellar evolutionary tracks for a solar-mass star. The models and selected parameters are: [M/H]=0, Y=0.282, α=1.9 (Baraffe et al., 1998); Y=0.28, Z=0.02 (Siess et al., 2000); Y=0.288, Z=0.02, α=1.68 (Tognelli et al., 2011); [M/H]=0, Y=0.28, α=1.6 (Baraffe et al., 2015). Here, [M/H] is the metallicity, Y the helium content, Z the metal content, and α the mixing length parameter. We extract ages and luminosities from all tracks and calculate the equilibrium temperature evolution for full redistribution and zero albedo at orbits of 1 AU and 0.7 AU. As shown in Fig. 2 we find temperature ranges at the age of ≈2, 5 and 10 Myr between the different models of ≈280 K, 248 K, 228 K (Earth) and ≈350 K, 297 K, and 277 K (Venus), respectively, in agreement with the two most recent models (Baraffe et al., 2015; Tognelli et al., 2011).

For the calculation of r_{ph}, for assumed initial protoplanet masses of 0.45 - 0.8M_{Earth}, we calculated hydrodynamic atmospheric models in a similar way as described in detail in Fossati et al. (2017) and Kubyshkina et al. (2018b) with the aim of deriving the hydrogen "boil-off" escape fluxes F_{th} for these protoplanetary masses at Venus and Earth orbit. During this initial extreme escape phase the photospheric radius of the planet shrinks fast until the planet reaches a "stable" configuration.

To define the photospheric radius r_{ph} and corresponding escape rate of the planet coming out of the "boil-off" phase, for each protoplanetary mass considered in this study we assign a set of possible photospheric radii. For each pair of M_{proto}, r_{ph} we

applied 1D hydrodynamical modelling following Erkaev et al. (2015); Fossati et al. (2017); Kubyshkina et al. (2018b) and use the resolved atmospheric parameters to define a posteriori the actual photospheric radius. The model solves the system of basic hydrodynamic equations

$$\frac{\partial \rho}{\partial t} + \frac{\partial(\rho v r^2)}{r^2 \partial r} = 0, \tag{1}$$

$$\frac{\partial \rho v}{\partial t} + \frac{\partial[r^2(\rho v^2 + P)]}{r^2 \partial r} = -\frac{\partial U}{\partial r} + \frac{2P}{r}, \tag{2}$$

$$\frac{\partial[\frac{1}{2}\rho v^2 + E + \rho U]}{\partial t} + \frac{\partial v r^2[\frac{1}{2}\rho v^2 + E + P + \rho U]}{r^2 \partial r} = Q_{EUV} - Q_{Ly\alpha} + \frac{\partial}{r^2 \partial r}\left(r^2 \chi \frac{\partial T}{\partial r}\right) - Q_{H^+}, \tag{3}$$

where ρ, v and T are, respectively, the mass density, bulk velocity and atmospheric temperature as functions on the radial distance r from the center of the planet. U is a gravitational potential accounting for the Roche lobe effect (Erkaev et al., 2007). P and E are atmospheric pressure and thermal energy, respectively, and χ is a thermal conductivity of the neutral gas (Watson et al., 1981). In the right-hand of the energy conservation equation (3), quantities Q_{EUV}, $Q_{Ly\alpha}$ and Q_{H^+} are the volume heating/cooling rates of EUV heating (Kubyshkina et al., 2018a), Lyα cooling (Watson et al., 1981) and H^+ cooling (Miller et al., 2013).

The system of equations (1)-(3) is complemented with continuity equations for the number density, accounting for the chemical reactions between molecular and atomic hydrogen, their ions and H_3^+, including ionization, recombination and dissociation. The full list of included chemical reactions, and more thorough description and discussion of the model can be found in Kubyshkina et al. (2018a).

The outputs from the model are the height profiles of the atmospheric parameters, including atmospheric temperature, mass density, bulk velocity, dissociation and ionization rates. From this, we can resolve the isotropic mass loss through the upper boundary $F_- = 4\pi r^2 \rho v$. This value includes both primary escape because of the plan-

etary low gravity and the escape induced from the stellar insolation. Assuming, that the EUV exposed part of the escape should not be very different from what is given by the energy-limited formula (F_{en}), we define the parameters (particularly r_{ph} for the known protoplanetary mass) of the planet when going out of "boil-off" as the ones corresponding to $F \approx F_{en}$. This approach defines our start parameter. The further evolution is then described with the energy-limited approach (Watson et al., 1981; Hunten et al., 1987; Zahnle and Kasting, 1986; Odert et al., 2018).

As for the other parameters, we considered a stellar mass of 1 M , stellar EUV flux evolution scenarios expected for the saturation level of young G-type stars (Tu et al., 2015), and orbital separation of 1 AU for early Earth and 0.7 AU for early Venus, respectively with corresponding values of T_{eq}. By applying a radiative-transfer transmission-spectrum model[1] for a solar composition atmosphere and the temperature-pressure profiles obtained from the hydrodynamic code extended with isothermal hydrostatic profiles at high pressures, it is found that the optical depth $\tau = 1$ and thus r_{ph} lies for the mass-range of the studied protoplanets at ≈700 mbar (Cubillos et al., 2017; Kubyshkina et al., 2018b).

The initial atmospheric mass fraction of the captured H_2-envelope f_{at} remaining from the "boil-off" phase is estimated by using the initial model integrator of the TAPIR- Code (short for The adaptive, implicit RHD-Code) (Stökl et al., 2016; Johnstone et al., 2015; Stökl, 2008; Stökl et al., 2015; Lammer et al., 2014). The TAPIR-Code provides a framework for the implicit solution of the equations of radiation hydrodynamics on adaptive grids and previously has been applied to spherical flows (Dorfi et al., 2006), 2-dimensional flows (Stökl and Dorfi, 2007), convection modeling in Cepheids (Stökl, 2008), and planetary atmospheres (Erkaev et al., 2014; Lammer et al., 2014). To solve the hydrostatic structure equations of Stökl et al. (2015, 2016) we are taking into account radiative and convective energy transport, including the opacities for gas and dust, and

[1]https://github.com/exosports/BART

the flux of energy from the protoplanet. The dependence of r_{ph} on the atmospheric mass fraction $f_{at} = M_{at}/M_{pl}$ for protoplanetary masses of 0.45-0.81M_{Earth} obtained with this model can be described as

$$f_{at} = \left(\frac{\log(r_{ph}) + 0.07151}{1.14767} \right)^{-3.1217} , \tag{4}$$

with r_{ph} normalized to the Earth-radius. When the protoplanet accretes further mass, r_{ph} decreases with time, due to

$$\log(r_{ph}) = 1.14767 \cdot \left(\frac{M_{at}}{M_{pl}} \right)^{-3.1217} - 0.07151 . \tag{5}$$

2.2. Initial elemental abundances

If the protoplanets already accreted to masses that could attract H_2-envelopes within the protoplanetary disk, then one can expect that this atmosphere initially contained the elements and their ratios in solar abundances as given in Table 1. We consider every atmospheric element abundance a_{el} relative to the abundance of hydrogen a_H (Anders and Grevesse, 1989; Heber et al., 2012; Meshik et al., 2014; Lodders et al., 2009). From those we are then able to compute the total mass of each specific element in the H_2-envelope by $m_{el} = (a_{el}/a_H)M_{at}\,A$, where A is the atomic mass number of the element.

The solar wind provides information on the isotopic composition of the solar atmosphere, the bulk Sun and hence the protoplanetary nebula. For the initial abundance ratios of $^{36}Ar/^{38}Ar$ and $^{20}Ne/^{22}Ne$ shown in Table 1, we use data from the modern solar wind obtained by NASA's Genesis spacecraft (Heber et al., 2012; Meshik et al., 2014) and data that may represent the early solar wind that was trapped in solar gas rich soils and breccias on the Lunar surface and meteorites (lunar and meteoritic mineral grains: LMMG) (Anders and Grevesse, 1989; Pepin et al., 1999; Palma et al., 2002; Caffee and Nishiizumi, 2001; Lindsay et al., 2014). Since solar wind isotopes can

also be fractionated during solar wind formation and acceleration, we also consider Ar and Ne isotope ratios for the bulk Sun, represented by the so-called Outer Convective Zone (OCZ) derived by a model applied to Genesis data by Heber et al. (2012). Ini- tial noble gas ratios and abundances for different reservoirs compared to the measured present-day values of Earth and Venus are shown in Table 1; K/U ratio and abundances in Table 2, respectively. For the present day ratios of K/U we use the BSE ratio for Earth (Arevalo et al., 2009; Lodders et al., 2009); for Venus we use ratios inferred from surface rock-measurements by several Soviet landers. Besides solar, Earth, and Venus, we use admixtures of the following different compositions for the impacting material in our simulations, i.e. from the CC-reservoir

- an average of carbonaceous chondrites (CC), i.e. of CI, CM, CO, and CV chondrites (Marty, 2012; Wasson and Kallemeyn, 1988) and
- CI chondrites (CI) (Lodders et al., 2009),

and

- ureilite-like material (UR) (Rai et al., 2016; Göbel et al., 1978; Wasson and Kallemeyn, 1988; Workman and Hart, 2005; Gale et al., 2013) and
- enstatite-like material (EC) (Wasson and Kallemeyn, 1988; Patzer and Schultz, 2001, 2002).

from the NCC-reservoir.

For proto-Earth, we assume a wide range of different CC-NCC compositions in- cluding the suggested admixtures of Marty (2012), Dauphas (2017), and Schiller et al. (2018).

2.3. Magma ocean depth estimates

Schaefer and Fegley (2010) and Fegley et al. (2016) used chemical equilibrium and chemical kinetic model calculations for studying volatiles that are released by

Table 1: Initial ratios and abundances of Ne and Ar for different reservoirs. The solar values are in 1 n_H, the rest in mol/g.

Reservoir	$^{20}Ne/^{22}Ne$	$^{36}Ar/^{38}Ar$	^{20}Ne	^{36}Ar
Solar [SW]	13.77 [a]	5.50 [d]	6.13×10^{-5} [a]	1.45×10^{-6} [a]
Solar [LMMG]	13.69 [b]	5.79 [b]	2.29×10^{-3} [e]	1.097×10^{-4} [e]
Solar [OCZ]	13.34 [c]	5.33 [c]	6.13×10^{-5} [c]	1.45×10^{-6} [c]
CC	8.50 [f]	5.32 [f]	1.38×10^{-11} [f]	3.47×10^{-11} [f]
CI	9.02 [g]	5.32 [g]	8.10×10^{-12} [h]	3.11×10^{-11} [h]
UR	10.7 [i]	5.26 [i]	4.03×10^{-15} [j]	2.72×10^{-15} [j]
EC	10.48 [k]	4.89 [k]	4.66×10^{-10} [k]	2.69×10^{-11} [k]
Earth	9.8±0.008 [f]	5.32±0.33 [f]	2.22×10^{-13} [f]	9.58×10^{-13} [f]
Venus	11.8±0.7 [l]	5.6±0.6 [m]	–	–
	14.29±4.08 [n]	5.08±0.05 [n]	–	–

[a]Genesis solar wind data (Heber et al., 2012); [b]Solar wind data inferred from Lunar and meteoritic Mineral grains (LMMG) (Anders and Grevesse, 1989; Pepin et al., 1999; Palma et al., 2002); [c]Genesis data correlated to the Outer Convective Zone (OCZ) which is assumed to be similar to the solar nebula (Heber et al., 2012); [d]Genesis solar wind data from Meshik et al. (2014) – 5.47 in Heber et al. (2012); [e]Particles relative to hydrogen (n_H) - solar wind and OCZ data from Heber et al. (2012), LMMG data from Anders and Grevesse (1989); [f] Data from Carbonaceous Chondrites (CC) by Marty (2012); [g]Data from CI chondrites (CI) by Mazor et al. (1970); [h]Mazor et al. (1970) & Lodders et al. (2009); [i]Data from ureilites (UR) by Göbel et al. (1978); [j]According to Rai et al. (2016) the composition of the ureilite-like material can be assumed to be similar to the terrestrial depleted mantle (DM), i.e. for the abundances of ^{22}Ne and ^{36}Ar in UR we use the corresponding data for the DM as given in Marty (2012); [k]Data from Enstatites (En) by **Patzer and Schultz (2001, 2002)** (averaged); [l]Venera 13 & 14 (Istomin et al., 1983); [m]Pioneer Venus Orbiter (Hoffman et al., 1980; Donahue, 1986); [n]Venera 11 & 12 (Istomin et al., 1980).

Table 2: Initial ratios and abundances of K and U for different reservoirs. The solar values are in 1/ n_H, the rest in mol/g.

Reservoir	K/U	K
Solar	64,641 [a]	4.91×10^{-6} [b]
CC	38,825 [c]	1.03×10^{-5} [c]
CI	68,928 [d]	1.39×10^{-5} [d]
UR	12,340 [e]	1.04×10^{-6} [e]
EC	80,789 [c]	3.68×10^{-6} [c]
Earth	13 800 ± 2 600 [f]	–
Venus	7 032 ± 1 220 [g]	–
	18 182 ± 7 951 [h]	–

[a]Anders and Grevesse (1989); [b]Particles relative to hydrogen in the solar nebula/hydrogen atmosphere (Anders and Grevesse, 1989); [c]Carbonaceous chondrites (CC) assumed to be an average over CI, CM, CO, CV. Data from Wasson and Kallemeyn (1988); [d]Lodders et al. (2009); [e]According to Rai et al. (2016) the composition of the ureilite-like material can be assumed to be similar to the terrestrial depleted mantle (DM), i.e. for the abundance of K in UR we use the corresponding data for the DM as given in Workman and Hart (2005) and Gale et al. (2013); [f]Arevalo et al. (2009); [g]Vega 1, 2 & Venera 9, 10 landing sites (Davis et al., 2005); [h]Venera 8 landing site (Davis et al., 2005).

heating different types of carbonaceous, ordinary and enstatite chondritic material as a function of temperature and pressure. Their results predict significant amounts of S, P, Cl, F, Na, and K in accretionary atmospheres at high temperatures of ≈1500-2500 K by outgassing of magmatic material. During the early stage of atmosphere evolution, surface temperatures below the H_2-envelope can reach up to ≥2000-3000 K (Ikoma and Genda, 2006; Bouhifd and Jephcoat, 2011; Stökl et al., 2016), i.e. magma oceans will be present below the hydrogen atmosphere.

We considered protoplanets with masses between $0.5M_{\mathrm{Earth}}$ and $0.81M_{\mathrm{Earth}} = M_{\mathrm{Venus}}$. We further assumed the protoplanets to be differentiated into a silicate mantle and a metallic core and to have an Earth-like composition with core and mantle mass fractions of 32.5% and 67.5%, respectively (Valencia et al., 2006). For surface temper- atures between ≈2000-3000 K, such as those assumed in this study, at least part of the mantle lies largely above the liquidus and thus forms a magma ocean. Silicate liquids have low viscosity (Karki and Stixrude, 2010). The magma ocean is thus expected to undergo turbulent convection and hence to be well mixed and have an adiabatic tem- perature profile. For both peridotitic (Fiquet et al., 2010) and chondritic (Andrault et al., 2011) mantle compositions, the slope of the liquid adiabat is steeper than the slopes of the liquidus and solidus throughout the pressure range of the Earth's mantle (e.g., Monteux et al., 2016; Nikolaou et al., 2019). The mantle remains thus molten from its surface down to a certain depth and starts to solidify at its bottom, although, for a pure bridgmanite composition, crystallization could also begin at mid-mantle depths (Stixrude et al., 2009). Even when the temperature drops below the liquidus at depth upon mantle cooling, the magma ocean is expected to exhibit a liquid-like convective behaviour as long as the melt fraction is above a critical threshold of ∼40%, which marks a transition to the solid-like behaviour characteristic of creep deformation (Costa et al., 2009). Assuming that the surface temperature and the mantle potential temperature are similar (Lebrun et al., 2013), a condition satisfied

in the presence of the steam atmosphere that is likely to be outgassed by a magma ocean (Hamano et al., 2013), we computed the depth of the magma ocean based on the intersection between the adiabatic temperature profile and the temperature corresponding to the critical melt fraction of 40%. For different potential temperatures, we computed adiabatic profiles (T_a) according to the adiabatic gradient

$$\frac{dT_a}{dP} = \frac{\alpha T}{\rho c_P}, \tag{6}$$

where P is the hydrostatic pressure in GPa, c_P=1000 J kg^{-1} K^{-1} the heat capacity at constant pressure, and α the pressure-dependent thermal expansivity (Abe, 1997)

$$\alpha(P) = \alpha_0 \cdot \left(\frac{PK^J}{K_0}\right)^{\Sigma(1-K^J)/K^J}, \tag{7}$$

where $\alpha_0=3\cdot10^{-5}$ K^{-1} is the thermal expansivity at zero-pressure, K_0=200 GPa the bulk modulus, and K^J=4 its pressure-derivative. For the solidus and liquidus temperatures we assumed a peridotitic composition based on experimental data for pressures up to 22.5 GPa (Zhang and Herzberg, 1994; Herzberg et al., 2000) and for higher pressures (Fiquet et al., 2010) down to the core-mantle boundary. For the given surface temperature, the differences in the magma ocean depth between the studied protoplanetary masses range from a few percent to about 30%. As an example if one takes a protplanet of ≈0.5M_{Earth} with a surface temperature ranging from ≈2000-2600 K, the magma ocean depths can range from 135 - 1900 km. Thus, we assume an average depth of a magmatic layer of ≈1000 km for the protoplanetary masses considered in our study, from which the noble gases as well as potassium will be outgassed into the surrounding envelope. Depending on the actual composition of the magma ocean, its pressure range and degree of crystallinity, the residual melt can become denser than newly formed crystals due to strong FeO enrichment in the liquid phase (Caracas et al., 2019). Crystals and melt would thus tend to separate leading to an inside-out crystallization and the

formation of a basal magma ocean (e.g., Labrosse et al., 2007; Ballmer et al., 2017; Caracas et al., 2019). Yet, even in this case, the surface magma ocean would still be in contact with the surrounding atmosphere so that our assumptions would remain valid.

According to magma ocean studies the convective velocities in the magma ocean reach up to 10 m s^{-1} Solomatov (2007). Therefore, one can assume that 1000 km deep magma oceans are well mixed and soluble elements reach the protoplanetary surface from the bottom within a day. Because, of this short time scale one can assume that the escape of evaporating elements will not deplete the surface layer and elements can outgas from the magma ocean into the escaping primordial atmosphere to maintain the chemical equilibrium (Fegley et al., 2016).

We estimate the maximum amount of outgassed elements (i.e., K, Ar, Ne, etc.) from an average magmatic layer of ≈1000 km, which lies within the simulated magma ocean depth ranges, by assuming that they have been incorporated during the disk phase into the magma initially with compositions as described above (see Table 1 and references therein for different Ar and Ne noble gas ratios and abundances in CI/CC and UR; respectively Table 2 for K and U.).

1D radiative convective models of hot steam atmospheres above a solidified magma ocean (Marcq, 2012; Marcq et al., 2017) indicate that in later stages, after the H_2-dominated envelope was lost and large impacts decrease, mesospheric temperatures remain always lower than T_{eq}, even for very high surface temperatures and dense atmospheres. This severely hampers further escape of K and similar heavy elements once the primordial atmosphere is lost, the kinetic energy supply by impactors becomes negligible, and steam atmospheres are catastrophically outgassed.

However, additional enrichment of elements in the protoplanetary atmosphere can also be caused by the evaporation of impacting chondrites in the atmosphere, water production through oxidation of atmospheric hydrogen (Ikoma and Genda, 2006), as

well as due to large impactors crashing into the magma ocean that release their volatile materials (e.g., H_2O, CO_2) via shock degassing (Abe and Matsui, 1985). For investigating how additional volatiles influence the escaping hydrogen and the related elemental fractionation, we add different H_2O and CO_2 partial pressures within ranges of 15-75 bar and 1-15 bar respectively to the nebula-captured H_2-envelope.

2.4. Impact simulations

For simulations in which the initial protoplanetary masses are small enough we accrete the rest of the planet by adding giant impactors with different masses. To quantify atmospheric erosion by these giant impact-events, we performed 3D Smooth Particle Hydrodynamics (SPH) simulations of the growing protoplanets with captured H_2-envelopes being hit by Moon- and Mars-mass embryos.

Atmospheric loss due to impacting bodies has so far been treated by means of analytical models (Schlichting et al., 2015), 1D (Genda and Abe, 2003; Inamdar and Schlichting, 2016) and 3D hydrodynamic codes (Shuvalov, 2009) and of head-on impacts of Earth-sized onto super-Earth-sized planets (Shang-Fei et al., 2015). To quantify atmospheric losses in large impact events, we performed a suite of fully 3D SPH collision simulations considering two main scenarios. These comprise protoplanets between 0.6 and 0.75 M_{Earth} that are hit by either a Moon- or a Mars-mass planetary embryo with varying impact velocities and angles. Both colliding bodies consist of an iron core that contains 30 % of the total mass and a silicate mantle. The target body, representing the protoplanet, is covered by an H_2-envelope with f_{at} of ≈0.001, while the smaller impactor itself has no atmosphere. Fig. 3 shows collision snapshots of a Moon-mass planetary embryo that collides with an H_2 envelope surrounded protoplanet with $0.6 \times M_{Earth}$.

Our multi-material SPH code (Schäfer et al., 2016) includes self-gravity and runs on highly-parallel GPU hardware to allow for fast, high-resolution computations. Several material models and equations of state (EOS) are available, allowing simulation of gases, non-viscous fluids (Burger et al., 2018), granular media (Schäfer et al., 2017),

solid bodies (Maindl et al., 2014; Burger and Schäfer, 2017), and porous continua (Haghighipour et al., 2018). Due to the high involved masses, material strength is neglected in this study and the colliding bodies are modeled purely hydrodynamically. The core and mantle material are described by the Tillotson EOS (H. Tillotson, 1962), with parameters for iron (Melosh, 1989) and basalt (Benz and Asphaug, 1999) while the atmosphere is modeled as an ideal H_2 gas with an adiabadic index of 7/5. In order to produce equilibrated initial configurations we first compute hydrostatic profiles with a semi-analytical relaxation approach, as described in Burger et al. (2018), followed by additional numerical relaxation to settle remaining fluctuations. The outer boundary conditions for hydrostatic structure calculations were chosen to end up with atmospheric heights roughly half the radius of the underlying core and mantle.

To verify the influence of an evolving protoplanetary mass, four selected scenarios (Mars-sized projectile, v/v_{esc}=1.5, α=0°, 30°, 45°, 75°) were studied between masses of ≈0.6M_{Earth} and ≈0.75M_{Earth}, but all other collision parameters are equal. These scenarios led to atmosphere losses identical, or only marginally below those of the runs with less massive targets. Under the assumption of a constant bulk density ϑ, the specific collision energy Q_R as a function of v/v_{esc}, the total colliding mass M_{tot}, and $\gamma = M_{proj}/M_{targ}$ can be expressed as Burger et al. (2018)

$$Q_R = G \cdot \frac{4\pi\vartheta}{3}^{1/3} \cdot \frac{v}{v_{esc}}^{2} \; M_{tot}^{2/3} \frac{\gamma}{(\gamma + 1)^{5/3}(\gamma^{1/3} + 1)} \cdot \qquad (8)$$

On the one hand, the larger gravity of the more massive protoplanet can be expected to exert a stronger hold on the atmosphere, while on the other hand Eq. 8 indicates that the specific collision energy increases for higher M_{tot}, but also decreases for lower γ (which is both fulfilled for the ≈0.75×M_{Earth} runs compared to the respective 0.6×M_{Earth} runs). At least in the examined scenario these contributions seem to practically balance each other and atmosphere losses appear to be almost independent of the protoplanetary mass within the studied range.

By covering the full range of possible impact angles from central to almost perfectly grazing, and likely impact velocities from 1-2v_{esc}, as illustrated in Fig. 4 we infer on average atmosphere losses around 5% per collision for impacts with Moon-mass embryos and ≈15% for Mars-mass impactors. Besides this atmospheric mass loss one should note that these impactors also deliver mass and elements to the growing protoplanet. Impact masses with different $^{36}Ar/^{38}Ar$, $^{20}Ne/^{22}Ne$, and K/U ratios are thus added to simulate the growth of the protoplanet to its final mass as well as its elemental modification in the atmosphere. We varied the impactor composition to take into account different compositional models of the Earth. The Moon-forming impact as final impactor is assumed to not significantly alter the composition of proto-Earth.

To test the influence of varying atmosphere mass, we repeated all 10 simulations involving Moon-sized impactors with a significantly more massive atmosphere with f_{at}≈0.03, and found results very close to those of the standard runs, with deviations not larger than ≈1%. In addition, we also repeated one scenario (Mars-sized projectile, v/v_{esc}=1.5, α=30°) with a lower-mass atmosphere of ≈0.01 mass%, where 22% of the initial atmosphere is lost (vs. 16% in the standard run). The presence (or absence) of these deviations is at least partly due to different atmospheric heights, which certainly depend on various atmospheric properties, and the results derived from our standard runs should be considered as being not more than first order estimates.

Finally, to test resolution dependence, we repeated one scenario (Mars-mass projectile, v/v_{esc}=1.5, α=30°) in high resolution with 1 million SPH particles, instead of the 2.0-2.5×10^5 particles of the standard runs. The outcomes of the two simulations were found to be practically identical in all their major aspects.

For each collision we subtract a randomly determined atmospheric mass fraction, within 1-10% for Moon-mass and 1-30% for Mars-mass impactors. Frequent large impactors are also significant atmospheric heating sources since they disturb the at-

mosphere (see also Fig. 3) and produce shock waves (Genda and Abe, 2003; Trigo-Rodríguez, 2013) so we assume that trace elements such as K can reach the thermosphere, where they can be dragged along and be partly lost along with the escaping H_2-dominated atmosphere.

2.5. Element fractionation by EUV-driven hydrodynamic escape

The main process related to the escape of "rare gases" and volatile elements in primordial atmospheres of planets is the dragging of heavy particles by EUV-driven hydrodynamic escape of H atoms that originate from the dissociation of H_2 and H_2O molecules (Zahnle and Kasting, 1986; Hunten et al., 1987; Odert et al., 2018; Pepin, 2006).

For Sun-like stars younger than ≈3.5 Gyr, the intrinsic spread in stellar rotation rates and corresponding high-energy emission is large (Tu et al., 2015). To study the dragging and fractionation of the noble gas isotopes and K/U, we model the atmospheric escape along different possible EUV-flux (100–920 Å) evolution tracks of the young Sun. At very young ages, the EUV emission is saturated at a roughly constant fraction of the star's bolometric luminosity ($L_{\mathrm{EUV}} \sim 10^{-3}\, L_{\mathrm{bol}}$, Christian and Athioudakis (2002)), lasting ≈5 Myr, 25 Myr and 225 Myr, for slow, moderate, and fast rotator tracks. Because the rotation rate of the young Sun is unknown, we model various evolution scenarios, based on the rotation rate distribution of young solar-like stars according to

Tu et al. (2015)

$$
\begin{aligned}
L_{\mathrm{EUV}} = \mathrm{EUV}_{\mathrm{law1}} &: 2.45 \times 10^{31} t^{-0.83} \\
\mathrm{EUV}_{\mathrm{law2}} &: 3.57 \times 10^{31} t^{-0.87} \\
\text{slow rotator} : \mathrm{EUV}_{\mathrm{law3}} &: 5.75 \times 10^{31} t^{-0.93} \\
\mathrm{EUV}_{\mathrm{law4}} &: 6.55 \times 10^{31} t^{-0.95} \\
\mathrm{EUV}_{\mathrm{law5}} &: 8.66 \times 10^{31} t^{-0.98} \\
\mathrm{EUV}_{\mathrm{law6}} &: 1.54 \times 10^{32} t^{-1.05} \\
\mathrm{EUV}_{\mathrm{law7}} &: 2.49 \times 10^{32} t^{-1.11} \\
\mathrm{EUV}_{\mathrm{law8}} &: 3.46 \times 10^{32} t^{-1.14} \\
\text{moderate rotator} : \mathrm{EUV}_{\mathrm{law}}9 &: 4.70 \times 10^{32} t^{-1.18} \\
\text{fast rotator} : \mathrm{EUV}_{\mathrm{law}}10 &: 1.2 \times 10^{36} t^{-2.15}
\end{aligned}
\tag{9}
$$

where t is the stellar age in Myr and L_{EUV} the EUV luminosity in erg/s. Here, the $\mathrm{EUV}_{\mathrm{law}}$ 3, 9 and 10 correspond to the slow, moderate and fast rotating young Sun in Tu et al. (2015).

The hydrodynamic H escape flux F_{H} from an H_2-dominated atmosphere, where the heavy major component is atomic O (from dissociated H_2O molecules) and "k" are the heavy minor trace species (k=^{36}Ar, ^{38}Ar, ^{20}Ne, ^{22}Ne, K, CO_2) that are embedded in the outflow, can be written as (Zahnle and Kasting, 1986; Hunten et al., 1987; Odert et al., 2018)

$$
F_{\mathrm{H}} = \frac{\beta^2 \eta F_{\mathrm{EUV}}}{4\Delta\Phi \left(m_{\mathrm{H}} + m_{\mathrm{O}} f_{\mathrm{O}} x_{\mathrm{O}} + \sum_{k=1}^{n} m_k f_k x_k \right)}, \tag{10}
$$

where $\Delta\Phi = GM_{\mathrm{pl}}/r_{\mathrm{ph}}$ is the gravitational potential, $f_{\mathrm{O}} = n_{\mathrm{O}}/n_{\mathrm{H}} \sim N_{\mathrm{O}}/N_{\mathrm{H}}$ and $f_k = n_k/n_{\mathrm{H}} \sim N_k/N_{\mathrm{H}}$ are the mixing ratios relative to the atmospheric light main species (here, H), with local number densities n and atmospheric inventories N. Here, m_k is the mass of trace species k and x_{O}, x_{k} are the fractionation factors (Odert et al., 2018). The escape fluxes of the dragged heavy species can therefore be written as $F_{\mathrm{O}} = F_{\mathrm{H}} f_{\mathrm{O}} x_{\mathrm{O}}$ and $F_k = F_{\mathrm{H}} f_k x_k$. Here, β is the ratio of $r_{\mathrm{EUV}}/r_{\mathrm{ph}}$ where r_{EUV} is the effective radius where the bulk of the

incoming EUV radiation is absorbed.

The dynamics of hydrodynamically escaping H_2-dominated atmospheres with applications to the evolution of Venus and Earth were discussed by Watson et al. (1981). Under the studied conditions, it was found that the EUV-driven hydrodynamic escape of H atoms from the upper atmosphere of early Venus and Earth would have been energy-limited, corrected by a less than unity heating efficiency (Watson et al., 1981; Shematovich et al., 2014) η of 15%, if their primordial atmospheres contained total H_2 mixing ratios that exceeded a few percent. As one can see in Eq. 10, the hydrogen escape flux $F_H \propto r_{ph} r_{EUV}^2$ depends critically on r_{EUV}. We calculate the EUV absorption radius r_{EUV} numerically as Watson et al. (1981) in their pioneering work,

$$r_{EUV} = r_{ph}\Lambda_c \left\{ \frac{\Psi}{\Gamma_{max}} \left(\Lambda_c - \frac{2}{(1+s)\Gamma_{max}} \right)^{0.5} \right\}^{-0.5}, \tag{11}$$

with the quantity $\Psi = (\eta F_{EUV} G M_{pl} m_{H_2})/(T^{3/2}\kappa/k_B)$ and the maximum escape flux Γ_{max}

$$\Gamma_{max} = \frac{2}{1+s} \left\{ \left(\frac{\Lambda_c r_{ph}}{2 r_{EUV}} - \frac{1+s}{2} + 1 \right) \Lambda_c - \frac{\Lambda_c r_{ph}}{r_{EUV}} \right\}^{2}. \tag{12}$$

κ is the thermal conductivity parameter (Watson et al., 1981) of 4.45×10^4 ergs cm^{-1} s^{-1} K^{-1} and s the neutral gas factor of 0.7 (Banks and Kockarts, 1973). By solving Eq. 11 together with Eq. 12 simultaneously by numerical means new values of r_{ph}, r_{EUV}, f_{at}, M_{at} and F_H, F_O, F_k are determined, and the corresponding elemental fractionation ratios are calculated as a function of time.

In this approach atmospheric escape is limited by the amount of solar EUV energy absorbed in a narrow region around an effective EUV absorption radius r_{EUV} (Watson et al., 1981). However, it was shown by Erkaev et al. (2014, 2015) that this simplification yields for bodies with masses $< 1 M_{Earth}$ an underestimation of $r_{EUV} \approx r_{EUV_{min}}$ and thus

the escape rate. In such cases as illustrated in Fig. 5, due to the low gravity H_2- dominated low mass bodies develop extended upper atmospheres, so that the EUV flux is absorbed not in a narrow area but over a wide region above the photospheric radius r_{ph}, moving $r_{EUV_{eff}}$

$$r_{EUV_{eff}} \approx r_{EUV_{max}} = R_{ph} \left\{ 1 + 2 \int_{1}^{\infty} [1 - I_{EUV}(r, \pi/2)/F_{EUV}] r dr \right\}^{0.5}, \qquad (13)$$

to much higher distances (Erkaev et al., 2014, 2015), where $I_{EUV}(r, \theta)$ is the local stellar EUV flux in the atmosphere as a function of the non-dimensional radius $r = R/R_{ph}$ and spherical angle θ.

Because it is beyond the present study to calculate EUV-heated upper atmosphere structures of the accreting protoplanets by solving the full set of hydrodynamic equations at every evolution period we investigate the effect of r_{EUV} variations between a $r_{EUV_{min}}$ (Watson et al., 1981) and an $r_{EUV_{max}}$ based on hydrodynamic approaches (Erkaev et al., 2014, 2015) to the atmospheric loss rates from Eq. 10. To estimate an upper limit of $r_{EUV_{max}}$, we applied a hydrodynamic upper atmosphere model (Erkaev et al., 2016; Kubyshkina et al., 2018b) in the EUV-driven regime and assuming saturated solar EUV emission, which corresponds to the nebula lifetimes of 3-5 Myr (Wang et al., 2017; Bollard et al., 2017) of our simulation. Depending on the nebula lifetime, the corresponding equilibrium temperature, protoplanetary mass and EUV flux the difference between $r_{EUV_{max}} - r_{EUV_{min}}$ can amount to up to ≈1 Earth-radius.

The EUV flux F_{EUV} in Eq. 10 corresponds to $F_{EUV}=L_{EUV}/(4\pi d^2)$ with orbital distances d of 0.7 AU and 1 AU for Venus and Earth. We calculate the EUV-driven hydrodynamic atmospheric mass loss rate over time along various possible EUV luminosity L_{EUV} evolution tracks (Tu et al., 2015) shown in Fig. 6, which is defined as $\dot{M}_H=dM_H/dt=4\pi r_{ph}^2 m_H F_H$. The EUV flux, the mixing ratios and the fractionation factors are therefore calculated as functions of time. This provides the description of the evolving elemental masses m_{el} for the considered isotope and elemental ratios. From

the evolving elemental masses we build the various isotope and elemental ratios.

2.6. Fractionation factors and binary diffusion parameters

Since we aim to study the loss of H atoms that drag away O atoms (a dissociation product of H_2O), CO_2 molecules and the embedded trace elements ^{36}Ar, ^{38}Ar, ^{20}Ne, ^{22}Ne, and K, we apply a formalism for the calculation of the fractionation factors, which is applicable to more than two species. Here we apply improved analytic so- lutions (Zahnle and Kasting, 1986; Zahnle et al., 1990) of the general hydrodynamic multi-component equations (Hunten et al., 1987). These equations are applicable to atmospheres with one or two major species and an arbitrary amount of additional minor species (Zahnle and Kasting, 1986). Assuming that the escape of the heavier constituents is mainly driven by efficient hydrodynamic escape of species H, the frac- tionation factors x_O and x_k (k=^{36}Ar, ^{38}Ar, ^{20}Ne, ^{22}Ne, K) of the heavier species can then be written as (Zahnle and Kasting, 1986; Odert et al., 2018; Zahnle et al., 1990; Lichtenegger et al., 2016)

$$x = 1 - \frac{g\,(m_O - m_H)\,b_{H,O}}{F_H\,k_B T\,(1 + f_O)} \tag{14}$$

and

$$x_k = \frac{1 - \frac{g(m_k - m_H)b_{O,k}}{F_H k_B T} + \frac{b_{H,k}}{b_{H,O}} f_O\,(1 - x_O) + \frac{b_{H,k}}{b_{O,k}} f_O\,x_O}{1 + \frac{b_{H,k}}{b_{O,k}} f_O}, \tag{15}$$

Here, g is the gravitational acceleration at the base of the flow r_0, k_B is the Boltzmann constant, T the upper atmosphere temperature, and F_H the escape flux at r_{ph} of hydrogen in units of $cm^{-2}\,s^{-1}$. The binary diffusion parameters $b_{H,O} = 4.8 \times 10^{17} T^{0.75}\ cm^{-1}\,s^{-1}$, $b_{H,CO_2} = 8.4 \times 10^{17} T^{0.6}\ cm^{-1}\,s^{-1}$, $b_{H,Ar} = 1.06 \times 10^{18} T^{0.597}\ cm^{-1}\,s^{-1}$, $b_{H,Ne} = 7.9 \times 10^{17} T^{0.731}\ cm^{-1}\,s^{-1}$, $b_{O,CO_2} = 7.86 \times 10^{16} T^{0.776}\ cm^{-1}\,s^{-1}$, $b_{O,Ar} = 5.6 \times 10^{16} T^{0.841}\ cm^{-1}\,s^{-1}$ and $b_{O,Ne} = 1.5 \times 10^{17} T^{0.75}\ cm^{-1}\,s^{-1}$ were taken from Zahnle and Kasting (1986). The binary diffusion coefficients of potassium within hydrogen and oxygen $b_{H,K}$ and $b_{O,K}$ in units of $cm^{-1}\,s^{-1}$ are calculated from the relation (Koskinen

et al., 2013)

$$b_{\mathrm{H\,O\,K}} = 1.52 \times 10^{18}\left(\frac{1}{M_{\mathrm{H,O}}} + \frac{1}{M_{\mathrm{K}}}\right)^{1/2} \sqrt{T}. \quad (16)$$

Eq. 14 describes the fractionation of the major heavy species O and is similar to the frequently used expression derived by Hunten et al. (1987), except that it does not require that $f_{\mathrm{O}} \ll 1$. This expression is therefore more suitable for calculating the escape of dissociated H_2O products such as oxygen in the atmosphere. Eq. 15 describes the fractionation of the additional heavy minor species (here CO_2, ^{36}Ar, ^{38}Ar, ^{20}Ne, ^{22}Ne, K), which feel the drag from both major gases. If there is no heavy major species in the atmosphere, the escape of minor heavy species would be described by Eq. 14. The fractionation factors take values between 1 (both species escape efficiently with the same velocity) and 0 (the heavy species cannot escape). If the latter case occurs for the major heavy species, escape of the light species is then limited by diffusion through the static, heavy background gas, and its escape flux can be found from Eq. 14 by setting x_{O}=0. If x_k =0, the light gas still escapes hydrodynamically, but the concerned minor species is maintained.

2.7. Input parameters and χ^2 statistical tests

For constraining the upper limit of accreted masses during the disk lifetime of proto-Venus and Earth that can capture small primordial atmospheres and our model runs can reproduce the present atmospheric Ar, Ne isotope ratios within the measured error bars we vary input various input parameters discussed below and apply a statistical χ^2 test. The main input parameters of the applied upper atmosphere drag model are initial protoplanetary masses M_{pl}, the H envelope mass, the composition of the envelop and of the elements outgassed from the magma ocean, the evolution of the EUV radiation given as power laws (Eq. 9), EUV absorption radii within $^{\min} r_{\mathrm{EUV}}$, initial H_2O and CO_2 atmospheric partial pressure within the H_2-dominated gas envelope above the underlying magma ocean, the disk life time when the simulations start, and the times and $^{\max}$numbers of big Moon- (for Earth and Venus) or Mars-sized impacts (for

Earth only), and the composition of the impactors. In our study we investigated how these different parameters influence the model results. We defined a parameter grid where a range of values of the parameters are considered. The planetary mass grid for Earth ranges from 0.45-0.8M_{Earth} with increments of 0.01M_{Earth} masses. For Venus the planetary core mass grid ranges from 0.71 to 1.0M_{Venus} with increments of 0.01M_{Venus} masses. For core masses below the lower end of the planetary mass grids, no atmospheric mass can be kept gravitationally. For masses above the upper end of the planetary mass grid, none of the used EUV power laws can sufficiently drive atmospheric escape to fractionate the ratios down to present-day values. The EUV grid consists of 9 different EUV power laws (see Eq. 9, and Fig. 6), which were obtained by fitting additional laws between the three evolution tracks of Tu et al. (2015). The grid for the initial partial surface pressure ratios of H_2O/CO_2 are 5/1, 15/3, 30/6, and 75/15, respectively.

Important parameters are the photospheric radius r_{ph}, the equilibrium temperature T_{eq} at the planet's orbit, and the initial atmospheric mass M_{at} accreted from the solar nebula. To test whether variations of the parameter values influence the resulting fractionation of the elements, we also test different effective EUV absorption radii r_{EUV} between a minimum (Watson et al., 1981) and a maximum (Erkaev et al., 2014, 2015) value. For T_{eq} of proto-Venus and proto-Earth, we use temperatures for Earth of 245 K, and for Venus of 295 K. The initial M_{at} surrounding the planet is dependent on the protoplanet mass, T_{eq}, and the photospheric radius r_{ph}.

To determine the parameters (initial protoplanetary mass when the dissipated, EUV flux, H_2O/CO_2, t_{disk}, r_{EUV}, impactor scenarios), which best reproduce the presently measured isotope and elemental ratios of both Earth and Venus, we perform a χ^2 statistical test, which is defined by

$$\chi^2 = \sum_{pl=1}^{2} \sum_{k=1}^{3} \frac{(f_{k_{\mathrm{mod}}} - f_{k_{\mathrm{obs}}})^2}{f_{k_{\mathrm{err\,obs}}}^2}, \tag{17}$$

where $f_{k_{mod}}$ denotes the modelled isotope ratios, $f_{k_{obs}}$ the corresponding measured present-day isotope ratios, and $f_{k^{err}_{obs}}$ the error of the measured isotope ratios. Index *pl* refers to the planets, Earth and Venus, and index *k* refers to the element ratios that we use in the current study. The sum for index *pl* for Earth and Venus is done only for models with the same EUV power-law tracks and t_{disk} . For the χ^2 plot, we fix the planetary core mass grid and the EUV grid and sum all H_2O/CO_2, t_{disk}, r_{EUV}, and impactor scenarios. Additionally we vary the initial and impacting compositions between different admixtures of the CC- and NCC-reservoirs.

In this statistical method the sampling distribution of the test statistic is a χ^2 distribution when the null hypothesis is true. Therefore the lowest χ^2 values represents the best case.

3. Results

3.1. Statistical outcomes

The χ^2 model results shown in Fig. 7 present protoplanetary masses at the end of the disk lifetime vs. EUV evolution tracks (Fig. 6). Here, χ^2 values ≤5.0 corresponding to three reproduced elemental ratios for Earth and Venus, where the $^{36}Ar/^{38}Ar$, $^{20}Ne/^{22}Ne$ isotope and K/U ratios are within the present day ranges at the end of the evolution calculations. Values >5.0 indicate scenarios where at least one of the ratios is not within the error bars. Scenarios with χ^2 values >30.0 show distinct deviations from the present day measurements.

The simulations of Earth with low additional H_2O (5-75 bar) and CO_2 (1-15 bar) amounts and a disk life time of 5 Myr mark the lower limit for possible proto-Earth masses (≈$0.53M_{Earth}$) at the end of the disk phase retrieved from the distribution of χ^2 values where a tiny primordial atmosphere remained after the disk dispersal, whereas model runs with higher amounts of H_2O and CO_2 and disk life times of 3 Myr mark the upper limit of ≈ $0.58M_{Earth}$ for which the present atmospheric isotope ratios

can be reproduced. It has also to be noted that additions of partial pressures higher than 30 bar H_2O and 6 bar CO_2 respectively within the escaping hydrogen envelope cannot reproduce present day's measurements.

The addition of H_2O and CO_2 is less influential on Venus due to a more massive captured H_2-envelope. Here, a disk life time of 5 Myr ($0.85M_{Venus}$) marks the lower limit of proto-Venus masses as retrieved from the distribution of χ^2 values. The upper limit ($1M_{Venus}$) is obtained predominantly for EUV fluxes between a slow and moderate rotator (evolution tracks 3-9 in Fig. 6). In case of slower rotators proto-Venus did not grow up to its final mass within the disk lifetime. (evolution tracks 1-3 in Fig. 6). It is also interesting to note that Venus' mass and its corresponding captured H_2- envelope excludes that the young Sun was a moderate to fast rotating young G-star. A hypothetical reproduction of the atmospheric $^{36}Ar/^{38}Ar$, $^{20}Ne/^{22}Ne$ isotope and K/U ratios for these faster rotating young G-stars would need a higher mass for Venus so that a more massive primordial atmosphere could have remained after the boil-off phase. Because early Venus could not be more massive as today the planet's mass constrain the activity evolution of the young Sun if it captured a primordial atmosphere.

Thuerefore the χ^2 analysis in Fig. 7 indicates that the $^{36}Ar/^{38}Ar$, $^{20}Ne/^{22}Ne$ ratios and the measured present-day K/U elemental ratios on Venus and Earth can be reproduced if they captured small primordial H_2-dominated envelopes with proto-planetary masses of $\approx 0.83\text{-}1.0M_{Venus}$ and $\approx 0.53\text{-}0.58M_{Earth}$ if the EUV flux of the young Sun was within a slow (evolution track 3 in Fig. 6) to moderate (evolution track 9 in Fig. 6) rotating G-type star (Tu et al., 2015).

3.2. Possible evolution scenarios of early Earth and Venus

For the Earth, Fig. 8-**14** show examples where we could reproduce the atmospheric $^{36}Ar/^{38}Ar$, $^{20}Ne/^{22}Ne$ and today's observed BSE K/U ratios and some where either all three elements or at least one element could not be reproduced. In all cases we added $0.1M_{Earth}$ at 50 Myr, corresponding to the Moon-forming event with an Earth-

like composition via the giant impact caused by Theia (Canup, 2012). Fig. **15-16a** show evolution scenarios for an early Venus that captured a primordial atmosphere that can reproduce the atmospheric $^{36}Ar/^{38}Ar$, $^{20}Ne/^{22}Ne$ and today's observed Venus surface K/U ratios whereas Fig. 16b shows an attempt in which we cannot reproduce the ratios despite the large uncertainties in the available measurements.

An analysis of the different initial compositional reservoirs has shown that the captured H_2-envelope dominates the composition of the protoplanet to such an extent that we cannot distinguish any other reservoir that contributed to the protoplanet before the accreted primordial atmosphere is lost. In other words, whether we take 100% CC or CI, 100% UR or 100% EC, or a mixture as initial composition, it will always be overwritten by the solar component in the envelope. After the loss of the H_2-envelope, however, the composition of the impacting material starts to influence the results. We therefore only consider different compositions for the accreted mass after the primor- dial atmosphere is lost. Furthermore, changing initial atmospheric solar compositions between SW, LMMG, and OCZ (see Table 1) will not influence the results signifi- cantly within all uncertainties. In case of Ar the reason for this is that for successful reproduction attempts Ar underfractionates for all three initial solar composition val- ues due to the loss of the captured H_2-envelope, but the post-H_2-envelope impactors overwrite this fractionation partially. However, without the "accurateÂt'Ât' frac-
tionation through the escaping primordial atmosphere, the present-day $^{36}Ar/^{38}Ar$ ratio cannot be reached by overwriting an "inaccurateÂt'Ât' fractionation with the post-H_2-envelope impactors.

For post-H_2-envelope impactors with significant abundances of CC the present-day elemental and isotopic ratios can only be reproduced if these impactors are considered to be volatile-poor, i.e. depleted in the studied elements. Such an assumption is in agreement with studies of Erkaev et al. (2015) and Odert et al. (2018), and recently by Benedikt et al. (2019) who modeled the escape of volatile elements from Moon- to

Mars-mass planetary embryos. These studies showed in agreement with Young et al. (2019) that small Moon-mass embryos can lose a substantial amount of volatiles very rapidly. The amount of their loss is dependent on the orbit location, mass and surface temperature of the body as well as on the incident EUV flux. Furthermore, the depletion also depends on the mass and volatility of the elements, i.e. it can be expected that the noble gases will be stronger depleted than moderately volatile rock-forming elements. Also, within the noble gases, for small low-mass embryos the lighter Ne will be lost more efficiently than the heavier Ar (Benedikt et al., 2019). Here it is important to note that for small planetary embryos of up to Mars-size, even though noble gases such as Ar and Ne will escape from the magma ocean to space and therefore be depleted at such bodies, the isotopic ratios will not be affected due to the high loss rates as has been recently shown by Benedikt et al. (2019). While in case of the noble gases there is no significant difference for CCs and CIs, CIs have to be depleted in K and similar elements by about 50% more than for CCs to achieve the same results. Another way of depleting rock-forming elements could be impact erosion which tends to remove the crust of the embryo (see e.g. O'Neill and Palme (2008); Jellinek and Jackson (2015); Carter et al. (2015); Bonsor et al. (2015)). Nevertheless it seems to be unreasonable that planetary embryos will be much stronger depleted in rock-forming elements such as K compared to the noble gas Ar which has more or less the same mass range and a significantly lower condensation temperature.

In case of the post-H_2-envelope impactors it makes no difference whether we choose a few big impactors (e.g. in the range of M_{Mars}) or many small impactors (e.g. in the range of M_{Moon}) with the same composition and depletion as the few big ones to reach the final mass of proto-Earth and proto-Venus since there is no atmosphere left that could be eroded by the impacting material.

It is important to note that the present atmospheric $^{36}Ar/^{22}Ne$, which is ≈18.8 in today's atmosphere represents (Marty and Allé, 1994; Marty, 2012)a further constraint

on the composition of the accreted material of the post-nebula accretion.

3.2.1. Earth-case I (Dauphas, 2017): Composition derived from the isotopic nature of lithophile-siderophile elements

Fig. 8 shows examples for two evolution scenarios for early Earth in which we can reproduce the present-day atmospheric Ar and Ne isotope and the bulk K/U ratios with a protoplanetary mass of $0.55M_{\mathrm{Earth}}$ after a disk lifetime of 4 Myr and orbiting a young Sun that was less active than a moderate rotator with an EUV power law 7 (see Fig. 6) by assuming mainly accreting enstatite-like material as expected by Dauphas (2017). The differences between Fig. 8a and 8b are only due to a different enstatite-carbonaceous chondritic (EC-CC) mixture of the post-H_2-envelope impactor material.

The post-H_2-envelope impactor material in Fig. 8a consists of 95% EC that are highly depleted in noble gases and elements like potassium (K), and 5% CC that are weakly depleted. In such a case the CCs would have been delivered to early Earth mainly as undifferentiated meteorites.

Fig. 8b shows a case where the post-H_2-envelope impactor material consists of 70% EC and 30% CC-like material. Here the present atmospheric Ar, Ne and bulk K/U ratios can only be reproduced if the CC-like material is also highly depleted in the studied elements. In such cases the CC-like material should have been delivered via planetary embryos that underwent magma ocean-related outgassing followed by escape and hence depletion of these particular elements. Interestingly, for cases with post-H_2-envelope impactor material of < 70% EC and more parts of strongly depleted CC the atmospheric $^{36}Ar/^{22}Ne$ ratio can not reproduced anymore with the particular accretion scenario where early Earth accreted $\approx 0.7M_{\mathrm{Earth}}$ as long as it was surrounded by a primordial atmosphere (<7 Myr). For the cases shown in Fig. 8a and 8b this ratio yields ≈18.8 which matches the present-day atmospheric value (Marty and Allé, 1994; Marty, 2012). The scenario shown in Fig. 8a agrees

quite well with a composition obtained by Dauphas (2017) of an accreting EC-like material with a small addition of ≈ 5% CC and with the analysis of Marty (2012). The spike like features correspond to atmospheric delivery/losses and changes in the elemental ratios caused by large impactors.

Fig. 9 shows examples for an evolution scenario where we assume that the post-H_2-envelope impactors consist of 100 % EC-like material that is not depleted in Ar, Ne and K (Fig. 9a) and almost fully depleted in these elements (Fig. 9b). One can see that both scenarios cannot reproduce the present atmospheric Ar, N and bulk K/U ratios. This indicates that at least a few percent CCs must have been accreted after the loss of the tiny primordial atmosphere. This is also in agreement with the analysis by Marty (2012) which has shown that the $^{20}Ne/^{22}Ne$ end member (planetary-A) matches the composition of CCs and not of ECs and OCs.

Fig. 10 shows a similar scenario as that of Fig. 8a, but the influence of different EUV flux evolution tracks of the young Sun. Fig. 10a corresponds to a very slow rotating weakly EUV active young Sun (power law 1, see Fig. 6), while Fig. 10b shows a result for a moderately rotating and slightly more EUV active young Sun (power law 9) as that shown in Fig. 8a. One can see that a very slow rotating young Sun cannot reproduce present Earth's atmospheric Ar and Ne isotope ratios even though all assumptions except the EUV flux remained the same as in Fig. 8a. The $^{36}Ar/^{22}Ne$ ratio in Fig. 10a is far below the present atmosphere value. Less depleted EC-like post-H_2-envelope impactors in elements like K may yield the present bulk K/U ratio but Ar and Ne isotopes cannot be reproduced for this scenario.

Fig. 10b shows the same scenario as Fig. 8a but for a moderately rotating young Sun that was slightly more active in EUV compared to the scenario shown in Fig. 8a. Interestingly, the present atmospheric $^{36}Ar/^{38}Ar$ and $^{20}Ne/^{22}Ne$ isotope ratios and also the bulk K/U can be more or less reproduced. However, the present isotopic $^{36}Ar/^{22}Ne$ ratio can not reproduced under this conditions, although changes in

the depletion of the post-H_2-envelope impactor material will not produce accurate results.

Fig. 11a shows a scenario with similar proto-Earth and young Sun input parameters as in Fig. 10b but with an assumed post-H_2-envelope impactor com- position and depletion which can more or less reproduce the present atmospheric $^{36}Ar/^{22}Ne$. One can see that in such a scenario the atmospheric $^{20}Ne/^{22}Ne$ isotope ratio cannot be reproduced and the necessary depletion for the reproduction of the $^{36}Ar/^{22}Ne$ isotope ratio is very unrealistic. It is impossible that the post-H_2-nebula CC impactors will be undepleted in Ar but almost fully depleted in Ne isotopes.

Fig. 11b uses the same input parameters as given in Fig. 8b, but a post-H_2- envelope impactor composition of strongly depleted 98% EC and 2% CC that are not depleted. One can see that the $^{36}Ar/^{38}Ar$ and $^{20}Ne/^{22}Ne$ isotope ratios, as well as the bulk K/U ratio can be more or less reproduced, the atmospheric $^{36}Ar/^{22}Ne$ isotope ratio is too low. This more or less corresponds to the Marty (2012) case of an accretion consisting of 98% dry material and 2% undepleted CC, but with an escaping primordial atmosphere that alters the ratio. Consequently more than 2% CC are needed that show a slight depletion of Ne, if a hydrodynamic escaping primordial atmosphere was involved in shaping the present-day values.

3.2.2. Earth-case II (Schiller et al., 2018): Composition derived from Ca-isotopes in planetary embryos

The largest difference between the compositions given in (Dauphas, 2017) and (Schiller et al., 2018) is that (Schiller et al., 2018) suggests that the post-H_2-envelope impactors consisted mainly of carbonaceous chondrites, ≈60% dry ureilite-like material was accreted within the disk-lifetime. Fig. 12 shows examples for two evolution scenarios for early Earth in which we can reproduce the present-day ratios with a similar protoplanetary mass of $0.55M_{\mathrm{Earth}}$ after a disk lifetime of 4 Myr and **a similar** young Sun that was less active than a moderate rotator with an EUV power law

7.

Fig. 12a is basically equivalent with the result of Schiller et al. (2018), i.e. an accretion of 100% CI for the last ≈40% of proto-Earth. While Schiller et al. (2018), however, expects an accretion of about 100% CI for the last ≈40% of proto-Earth, we used an averaged value over all carbonaceous chondrites in Fig. 12a, ie. 100% CC. If one exchanges CCs with CIs then the depletion of K would have had to be slightly higher than the depletion of the more volatile noble gas Ar to reproduce the present-day ratio which might be unreasonable. Here, we can reproduce the present atmospheric Ar and Ne isotope ratios if we accrete more mass within the escaping H_2-dominated primordial atmosphere, which results in a faster growth of the proto-Earth. In such cases proto-Earth would have accreted ≈ $0.85M_{\mathrm{Earth}}$ as long as it was surrounded by an escaping primordial H_2-envelope (<7 Myr). The post-H_2-envelope impactors, however, have to be strongly depleted in the studied elements to reproduce the present-day ratios. Interestingly, such a fast growth was also derived by (Schiller et al., 2018) from their Ca-isotope analysis.

The main differences between Fig. 12a and 12b are only due to the delivered material of the post-H_2-envelope impactors. One can see that in both cases the atmospheric $^{36}Ar/^{22}Ne$ isotope ratio also yield the present-day atmospheric value of 18.8 (Marty and Allé, 1994; Marty, 2012). Fig. 12b has a post-H_2-envelope impactor composition of 70% CC and 30% UR and 30% of the total mass are delivered after the captured primordial atmosphere was lost to space. In such a slightly slower accretion scenario the impacting material has to be strongly depleted in noble gases; Ne for instance by ≈99%. Such strong depletion of the noble gases might also not be unrealistic since the present-day Earth has noble gas abundances that are about 2 magnitudes lower than those of undepleted carbonaceous chondrites (Marty, 2012).

Fig. 13 shows a similar scenario as that of Fig. 12a, but the influence of different EUV flux evolution tracks of the young Sun. Fig. 13a corresponds to a very slowly

rotating weakly EUV active young Sun (power law 1), while Fig. 13b shows a result for a moderatele rotating and slightly more EUV active young Sun (power law 9) as that shown in Fig. 12a. Similar as in the cases shown in Fig. 10 one can see that a very slow rotating young Sun can not reproduce the present atmospheric Ar and Ne isotope ratios if the assumption for the proto-Earth besides the activity of the young Sun remain similar as in Fig. 12a. The $^{36}Ar/^{22}Ne$ ratio is only 0.47 and is far below the present atmosphere value. Fig. 13b shows the same scenario as Fig. 13a but for a moderate rotating young Sun that was slightly more active in EUV compared to the scenario shown in Fig. 12a. Similar as in Fig. 10b, the present atmospheric $^{36}Ar/^{38}Ar$ and $^{20}Ne/^{22}Ne$ isotope ratios can be more or less reproduced. However, the present isotopic $^{36}Ar/^{22}Ne$ ratio, however, is too low.

Fig. 14 shows unsuccessful evolution scenarios where the proto-Earth accreted a higher mass of $0.75M_{\mathrm{Earth}}$ during the nebula lifetime. In Fig. 14a the growing protoplanet is exposed to a young Sun with an EUV flux that is a bit lower than that for a moderate rotator, similar as in Fig. 8a and 12a. One can see that the atmospheric $^{36}Ar/^{38}Ar$, $^{20}Ne/^{22}Ne$, $^{36}Ar/^{22}Ne$ noble gas ratios and the BSE K/U ratios can not be produced and Earth would not have lost its captured primordial atmosphere. Fig. 14b shows the same evolution scenario but exposed to a fast rotating early Sun. In such a case, due to the very high EUV flux the captured primordial atmosphere would have been lost within 500 Myr, but K/U and the atmospheric $^{36}Ar/^{38}Ar$, $^{20}Ne/^{22}Ne$, $^{36}Ar/^{22}Ne$ noble gas ratios never reached the present atmospheric values.

To summarize, it is also possible to reproduce the present atmospheric Ar, Ne and bulk K/U ratios by assuming the composition inferred by (Schiller et al., 2018) from the Ca-isotope data, if we assume a faster growth of proto-Earth as long as it is surrounded by its escaping primordial atmosphere and the accreting material is strongly depleted in the studied elements. However, the proto-Earth mass until the disk dissipated at ≈4 Myr should not be > $0.58M_{\mathrm{Earth}}$ and the process would

be a complex interplay between EUV-driven hydrodynamic and impact-induced atmospheric escape combined with a fast mass accretion soon after the time when the disk dissipated. If proto-Earth accreted higher masses of about 0.7-0.8 M_{Earth} during the disk lifetime than Earth would have had a problem to lose its primordial atmosphere and Ar and Ne isotope ratios can not be reproduced. This is also in agreement with studies of Johnstone et al. (2015); Owen and Wu (2016).

3.2.3. Venus: examples of different individual cases

Best case evolution scenarios for Venus are shown in Fig. 15. Here, Venus accreted more or less all of its mass until the captured primordial atmosphere was lost. For such scenarios (see Figs. 15 and 16) the assumed composition of proto-Venus has negligible effects on the results. In Fig. 15a, proto-Venus finished its accretion within the disk life time of 4 Myr to its full mass (i.e., $1.0M_{\mathrm{Venus}}$), and we assume the same solar EUV evolution track as for the best-case evolution scenarios of proto-Earth in Figs. 8a and 12a. The escaping hydrogen atoms dragged the trace species and fractionated initially solar-dominated $^{36}Ar/^{38}Ar$, $^{20}Ne/^{22}Ne$ noble gas ratios to values within the error ranges observed in today's Venus' atmosphere. For the particular scenario the atmospheric Ne isotope ratio lies within the measurement range of Venera 13 and 14 (Istomin et al., 1983; Donahue, 1986). Because of the large uncertainties of the presently available Ar isotope data, the $^{36}Ar/^{38}Ar$ ratio also lies within the error range. For this particular scenario the observed elemental ratios can be reproduced independently of the additional H_2O and CO_2 amounts discussed above. Here, proto-Venus accumulated a little bit earlier more nebular gas with solar composition compared to a less massive proto-Earth shown in Fig. 8a and 9a, so that impacting carbonaceous chondritic material did not modify the solar isotope ratios efficiently until accretion finished. The K/U ratio lies slightly above the Vega 1, 2 and Venera 9, 10 data but within the range of the Venera 8 landing site (Davis et al., 2005).

Gamma ray spectrometry data analysis of the rocks at the Venera 8 landing site

showed that the surface material contains relatively high contents of K, U, and Th (Vinogradov et al., 1973; Surkov et al., 1976). Abdrakhimov and Basilevsky (2002) used Magellan radar images of the Venera and Vega landing-site regions, and carried out a photogeologic analysis and mapping of these regions to interpret the soil composition, which was previously analyzed by the various spacecraft. Judging by the mapping results, a geochemically advanced material analyzed at the Venera 8 landing site appears to be a complex of shield plains (Abdrakhimov and Basilevsky, 2002). Anomalously high abundance of small volcanic shields were discovered on the Venera 8 landing site, which lead to the suggestion that the rocky material sampled by Venera 8 could represent these shields (Crumpler et al., 1997; Basilevsky, 1997). The formation of shield fields, instead of vast basaltic floods that are more typical for Venus, is believed to be due to low magma replenishment rates (Crumpler et al., 1997). These authors expect that these conditions might have favored intra-chamber magma differentiation and/or contamination in the crustal material, that enriched the sampled rocks by the Venera 8 in K, U, and Th (Basilevsky, 1997; Abdrakhimov and Basilevsky, 2002).

Fig. 15b shows a successful reproduction attempt that reproduce Venus' atmospheric Ar noble gas isotope ratio measured by Venera 11 and 12 mass spectrometer data (Istomin et al., 1980). In such an evolution scenario proto-Venus accreted less mass (i.e., $0.95M_{\mathrm{Venus}}$) within the nebula lifetime of 4 Myr and an EUV flux of the early Sun that is slightly lower compared to the scenario in Fig. 15a. Interestingly, here the obtained K/U ratio would lie within the narrow error bars measured by the Vega 1, 2 and Venera 9, 10 surface landers. The Vega 1, 2 and Venera 9, 10 data indicate Tholeiitic compositions, probably represent the unit of plains with wrinkle ridges, which is most common on Venus (Abdrakhimov and Basilevsky, 2002). Here, the evolution scenario is closer to that of the Earth shown in Fig. 8a or 9a. The ^{20}Ne/^{22}Ne ratios which are obtained in this particular scenario would lie outside the error bars of the measurements of Venera 13 and 14 (Istomin et al., 1983; Donahue, 1986), but very close to the lower

error bar of the initial PVO data analysis by Hoffman et al. (1980).

Fig. 16a shows a case of an even smaller proto-Venus with $0.83M_{\mathrm{Venus}}$ at the time when the disk evaporated at ≈4 Myr and a 100% EC composition, initially and delivered by the impacting material. Due to the large error bars of the available measurements the atmospheric Ar, Ne and also the surface K/U ratios can be reproduced. Fig. 16b shows an example of a failed reproduction attempt of the Venus' atmospheric Ar and Ne noble gas isotope and surface rock K/U ratios. A smaller proto- Venus that grows to its final mass before the captured primordial atmosphere escaped will lose most of its potassium for EUV evolution tracks higher than for a slowly rotating Sun. In this particular case K/U remains significantly under-fractionated.

In Venus' case different evolution scenarios yield a reproduction of the present day atmospheric Ar, Ne and also surface K/U ratio measurements. We agree with Dauphas (2017) that new precise measurements in future Venus missions are necessary so that one can test which material was mainly accreted by Venus and whether it can be linked to material related to EC, or a mixture of EC/CC with remnants from a primordial atmosphere.

3.2.4. $^{36}Ar/^{22}Ne$: a further constraint on the accreting material composition

As discussed above, different admixtures of UR, EC, and CC-like material of the post-H_2-envelope impactors can reproduce the present-day terrestrial atmospheric $^{36}Ar/^{38}Ar$ and $^{22}Ne/^{20}Ne$ ratios in dependence of their composition and assumed depletion. A further constraint for the composition of the post-nebula accretion is hidden in the atmospheric ratio of $^{36}Ar/^{22}Ne$ which is ≈18.8 in today's atmosphere (Marty and Allé, 1994; Marty, 2012). Fig. 17 shows the evolution of $^{36}Ar/^{22}Ne$ for reproduction cases based on the building block compositions suggested by (Dauphas, 2017) shown in Fig. 8a (95% strongly depleted EC, 5% weakly depleted CC), Fig 9a (100% non-depleted EC), and Fig 9b (100% strongly depleted EC), suggested by (Marty, 2012) – but with a tiny escaping H_2-envelope – shown in Fig. 11b (98%

strongly depleted EC and 2% non-depleted CC), and suggested by (Schiller et al., 2018) shown in Fig. 12a (100% depleted CC). As can be seen, only the Schiller-like case and the Dauphas-like case but with a post-H_2-envelope impactor contribution of about 5% CC can reproduce the present-day atmospheric $^{36}Ar/^{22}Ne$ ratio. As can also be seen in this figure, a contribution of 100% EC after the tiny primordial atmosphere was lost cannot reproduce the ratios correctly. One should also note that the depletions of the post-H_2-envelope impactor material can not be chosen completely arbitrarily. As shown in the example of Fig. 11a cases, where for instance only one noble gas is strongly depleted such as Ne but Ar and moderately volatile elements such as K are not depleted at all are physically not realistic (see also (Benedikt et al., 2019)). Therefore, in our case studies either all elements are not depleted or depleted and Ar and Ne should be higher depleted than K. Moreover, the heavier Ar isotopes should not be less depleted compared to the lighter Ne isotopes.

3.2.5. Fractionation of $^{41}K/^{39}K$, $^{66}Zn/^{64}Zn$ and Rb/U

In case of the Earth the present-day isotope ratio $^{39}K/^{41}K$ shows no significant fractionation (Wang and Jacobsen, 2016a,b) which should also be reflected in our results. In addition, the moderately volatile element Zn also does not show a significant fractionation between its isotopes (Herzog et al., 2009; Paniello et al., 2012).

To address this in our simulations, we show in in Fig. 18a the respective elements/isotopes for the same cases as in Fig. 17. Both modeled isotope ratios frac- tionate during the loss of the primordial atmosphere but this fractionation will then be overwritten and compensated by the post-H_2-envelope impacting material. For Zn the same depletions as for K (see Fig. 8a, 12a) were assumed. Another moderately volatile element that behaves similar to K is Rb (Lodders et al., 2009). Here, the present-day terrestrial Rb/U (Lyubetskaya and Korenaga, 2007) can only be reproduced very well by the Dauphas-like case of Fig. 8a with the same depletion of the post-H_2-

envelope impactors as for K. The cases either under or overfractionate Rb/U. The depletion of Rb might, however, not be the same as for K since Rb has on the one hand a lower condensation temperature than K, but on the other hand Rb is more than twice as heavy as K. This means that it might be outgassed easier but escapes less effectively from planetary embryos than the lighter K.

However, one should note that focusing only on these moderately volatile elements can lead to misleading interpretations. Including noble gas fractionation is therefore crucial for constraining post-H_2-envelope impactors.

If one simulates these ratios for the Venus best case scenarios with a large (Fig. 15a, Fig. 15b) and a small primordial atmosphere (Fig. 16a), one can see a remarkable difference between an almost fully accreted proto-Venus when the disk dissipated or a smaller proto-Venus that further accreted material after the primordial atmosphere escaped. For the almost fully grown proto-Venus $^{41}K/^{39}K$ and $^{66}Zn/^{64}Zn$ will be significantly fractionated by atmospheric escape, while for the smaller counterpart these ratios will be overwritten by the later impactors and almost no fractionation will remain. For Rb/U, on the other hand, the smaller proto-Venus will show a stronger fractionation than the heavier proto-Venus cases. Future missions to Venus may not only measure and prove these ratios but will therefore also be able to give an insight on Venus' accretion history, i.e. on whether Venus grew to its final mass already almost entirely within the disk lifetime or accreted slower.

4. Discussion

A common denominator in our simulations is that whether the initial composition of Venus and Earth at the time when the disk dissipated nor of the impactors accreted within the lifetime of their primordial atmospheres can be determined by our model runs. This is due to the reason that the solar-like component from the nebula, in particular of

the noble gases, within the captured H_2-envelope is dominating any information on the composition of the protoplanets. For impactors that are accreted after the H_2-dominated primordial atmosphere is lost, however, the composition is crucial for the reproduction of the studied element and isotope ratios. In addition, the main mass fraction of the post-H_2-envelope impactor material have to be volatile-poor, i.e. significantly depleted in the studied elements. As can be seen in Fig. 8a, in Earth's case as long as only a few percentage of CCs were involved in the post-H_2-envelope impactor material it could also be delivered mainly by undifferentiated meteorites.

For the Earth, with our method we can reproduce the present day measured atmospheric Ar and Ne noble gas isotope and K/U ratios in case that it accreted fast to $\approx 0.7 M_{\mathrm{Earth}}$, if we assume a composition as inferred by (Dauphas, 2017), and to $\approx 0.85 M_{\mathrm{Earth}}$ with a composition as inferred by (Schiller et al., 2018) as long as the growing proto-Earth was yet surrounded by the captured nebula gas. This captured H_2-envelope was lost due to the EUV flux of a slowly to moderately rotating young Sun within ≤7 Myr after formation of the Solar System.

Such a fast accretion scenario is in agreement with recent numerical models that reproduce the formation and growth from asteroids to planetary embryos and large protoplanets within the disk lifetime (Lambrechts and Johansen, 2012; Johansen et al., 2015; Birnstiel et al., 2016). It is expected that these scenarios evolve from a two stage process, where the first generation of accreting bodies form very fast by streaming instabilities followed by continuous growth that is dominated by the gas-drag in combination by the accretion of mm-sized particles for planetesimals with radii larger than about 200 km (Johansen et al., 2015). These model simulations result in a fast formation of Mars-sized embryos and even more massive protoplanets $\geq 0.5\ M_{\mathrm{Earth}}$ over typical disk lifetimes of ≤5 Myr (Bollard et al., 2017; McSween, 2013; Schiller et al., 2018).

Accretion models of terrestrial planets can also be constrained by the experimental technique of high-precision isotope ratio mass spectrometry of tungsten (W). The de-

cay of ^{182}Hf to ^{182}W via ^{182}Ta with a half-life of 9 Myr provides a kind of radiometric chronometer of planet formation processes (Harper et al., 1991; Halliday et al., 1996; Halliday, 2000). Hafnium and W are highly refractory and should be in chondritic proportions in early solar system bodies. Hafnium is a lithophile element and is partitioned strongly into the silicate fraction of a planet, while W is moderately siderophile and partitions preferentially into a coexisting metallic phase. As a consequence the Hf/W ratio is greatly perturbed by core formation. The chondritic Hf/W ratio of ~1.3 of the Earth has been internally fractionated by core formation because more than 90% of the Earth‘s W has sunk into its core.

The residual silicate portion in Earth‘s crust and mantle the BSE has a Hf/W ratio in the range between 10-40 (Newsom et al., 1996). If the fractionation of Hf from W caused by core formation takes place during the first few Myr of the accreting proto-Earth, i.e. the lifetime of ^{182}Hf, excess ^{182}W relative to other isotopes of W should develop in the silicate portion of a planet as a consequence of enhanced Hf/W. Conversely, early Solar System metals should be deficient in ^{182}W relative to chondritic atomic abundances if they segregated without further equilibration, before ^{182}Hf decayed. Therefore the magnitude of the W isotopic effects are broadly speaking an indication of the rates of accretion of planetesimals and planets, together with the timing of core formation (Halliday, 2000).

A comparison between accretion scenarios according to ^{182}Hf-^{182}W chronometry (see Fig. 19a) of terrestrial rocks after Wood and Halliday (2005) and Yu and Jacob- sen (2011) shows that our obtained initial protoplanetary mass accreted at ≈4-7 Myr would correspond to a Hf/W ratio that is ≈15, lies close to Yu and Jacobsen (2011), and supporting a rapid accretion and early core formation (Yin et al., 2002; Kleine et al., 2002; Yu and Jacobsen, 2011; Rudge et al., 2010; Kleine and Walker, 2017). Moreover, in such a fast accretion scenario which is also favored from our study, the time between the last two giant impactors on Earth could have been long enough to

allow a solidification of a magma ocean before the last giant impact (i.e. the Moon-forming event) and a subsequent condensation of a catastrophically outgassed steam atmosphere. In such case one could expect that a liquid ocean already formed before the Moon-forming event. One could speculate that the first magma ocean might have been more reduced than the one after the Moon-forming impact. The catastrophically outgassed atmosphere from the first magma ocean would therefore have been rich in H_2 and CO while the second should have been rich in H_2O and CO_2. This may be reflected in the preservation of the approximate carbonaceous chondritic D/H signature in the terrestrial sea water (Marty, 2012). This hypothesis would also be in agreement with a recent study of Pahlevan et al. (2019) who concludes from analysis of hydrogen isotopes that the observed oxidation of silicate Earth occurred before crystallization of the final magma ocean related to the late Moon-forming event.

Also a fast growth of proto-Venus during the disk phase is indeed indicated by i. the $^{20}Ne/^{22}Ne$ being closer to the solar value and ii. having higher abundances of the volatile noble gases compared to the Earth (and also to the smaller Mars) as can be seen in Fig. 19b (see also Pepin (1991)). Both indications might only be achieved with an initially higher mass of proto-Venus that could attract a larger H_2-envelope to counteract the higher EUV flux at closer orbit to the Sun.

The most likely evolution scenarios of early Venus and Earth, obtained from our model results are illustrated in Fig. 20. Proto-Venus accreted fast to about ≈0.65-0.81M_{Earth} (0.83-1.0 M_{Venus}) within the disk and captured more nebula gas compared to Earth, which was lost later. Earth grew only to ≈0.53-0.58M_{Earth} until the solar nebula dissipated, but grew fast to 0.70-0.85M_{Earth} as long as it was surrounded by the escaping H_2-dominated primordial atmosphere.

The evolution after proto-Earth lost its smaller H_2-envelope agrees with the hypothesis studied by Abe and Matsui (1985) where impactors crash into a global magma ocean until planetary accretion finished. After the impactor rate decreased the last

magma ocean solidified most likely after the Moon forming event and formed a catastrophically outgassed steam atmosphere (Salvador et al., 2017). Because of lower EUV fluxes, condensation of H_2O and ocean formation on Earth, and due to a much lower atmospheric hydrogen content, in Earth's case, heavy elements have not been further fractionated efficiently until today (Lammer et al., 2018).

Finally, it has to be noted that our simulations cannot exclude a scenario in which proto-Earth grew to masses < 0.5 M_{Earth}, but describes an alternative possibility and upper-mass constraint for a faster growing proto-Earth. If the planet grew slower, however, other explanations for the present-day atmospheric noble gas ratios than atmospheric escape have to be taken into account, such as the one outlined by Marty (2012).

5. Conclusions

Measured atmospheric $^{36}Ar/^{38}Ar$ and $^{20}Ne/^{22}Ne$ noble gas isotope and bulk K/U elemental ratios on Venus and Earth can be reproduced by a combination of EUV- driven hydrodynamic escape of H atoms from an initial nebular-based H_2-envelope and impacts, if

- proto-Venus and Earth were released from the nebula, after a disk lifetime of ≈4 Myr, with masses of ≈0.83-1.0M_{Venus} and ≈0.53-0.58M_{Earth}, and small H_2-envelopes,
- proto-Earth accreted ≈0.7-0.85M_{Earth} as long as it was surrounded by nebula gas within ≤7 Myr after the beginning of the Solar System,
- a slightly more massive solar-like H_2-dominated atmosphere most likely surrounded early Venus compared to the less massive proto-Earth, for which **enstatite and** carbonaceous chondrites modified the evolution of the noble gas ratios to today's measured atmospheric values, mainly reflected in the $^{20}Ne/^{22}Ne$ and $^{36}Ar/^{22}Ne$ ratios,

- the young Sun originated as a slowly to moderately rotating early G-type star.

The largest possible H_2-envelope on Venus can be captured during the disk lifetime if the planet accreted within this time period to its full mass. Under such conditions our results show that one can only reproduce Venus' $^{36}Ar/^{38}Ar$ and $^{20}Ne/^{22}Ne$ and bulk K/U ratios if the young Sun was less active than a moderate rotator. Thus, EUV fluxes corresponding to a faster rotating young Sun are very unlikely. Therefore, precise measurements by future Venus' space missions, of atmospheric noble gas isotope ratios and other elemental ratios distributed over a wide surface area would allow us to fine tune the evolution scenario of the planet and hence the Sun's history. Furthermore, our results are in agreement with ^{182}Hf-^{182}W chronometric accretion scenarios and a Hf/W ratio of <15 (Rudge et al., 2010; Yu and Jacobsen, 2011; Kleine and Walker, 2017).

Acknowledgements We acknowledge support by the Austrian Fonds zur Förderung der Wissenschaftlichen Forschung, Nationales Forschungs Netzwerk (FWF NFN) project S116-N16 and the subprojects S11603-N16, S11604-N16, S11606-N16, S11607-N16 and S11608-N16. H. Lammer, M. Leitzinger and Petra Odert acknowledge support of the FWF projects P27256-N27 and P30949-N36. D. Kubyskina, L. Fossati and H. Lammer acknowledge also the Austrian Forschungsförderungsgesellschaft FFG project "TAPAS4CHEOPS" P853993. N. Tosi and A. Nikolaou acknowledge support from the Helmholtz association (grant VH-NG-2017). H. Lammer also thanks Å. Nordlund from the Centre for Star and Planet Formation, University of Copenhagen, Denmark and M. Bizzarro from the Centre for Star and Planet Formation, University of Copenhagen, Denmark and Institut de Physique du Globe de Paris, France for fruitful discussions and advises related to the disk lifetime, terrestrial planet formation and initial composition of planetary building blocks. Finally we thank the two anonymous referees for their very valuable and important suggestions that helped to improve the results significantly.

Competing Interests The authors declare that they have no competing financial interests.

Correspondence Correspondence and requests for materials should be addressed to H.L. (email:

helmut.lammer@oeaw.ac.at).

References

Abdrakhimov AM, Basilevsky AT. Geology of the Venera and Vega Landing-Site Regions. Solar System Research 2002;36:136–59.

Abe Y. Thermal and chemical evolution of the terrestrial magma ocean. Physics of the Earth and Planetary Interiors 1997;100:27–39. doi:10.1016/S0031-9201(96)03229-3.

Abe Y, Matsui T. The formation of an impact-generated H_2O atmosphere and its implications for the early thermal history of the earth. In: Ryder G, Schubert G, editors. Lunar and Planetary Science Conference Proceedings. volume 15 of *Lunar and Planetary Science Conference Proceedings*; 1985. p. C545–59.

Albarède F, Blichert-Toft J. The split fate of the early Earth, Mars, Venus, and Moon. Comptes Rendus Geoscience 2007;339:917–27. doi:10.1016/j.crte.2007.09.006.

Anders E, Grevesse N. Abundances of the elements - Meteoritic and solar. Geochim Cosmochim Acta 1989;53:197–214. doi:10.1016/0016-7037(89)90286-X.

Arevalo R, McDonough WF, Luong M. The K/U ratio of the silicate Earth: Insights into mantle composition, structure and thermal evolution. Earth and Planetary Science Letters 2009;278:361–9. doi:10.1016/j.epsl.2008.12.023.

Avice G, Marty B, Burgess R, Hofmann A, Philippot P, Zahnle K, Zakharov D. Evolution of atmospheric xenon and other noble gases inferred from Archean to Paleoproterozoic rocks. Geochim. Cosmochim. Acta 2018;232:82–100. doi:10.1016/j.gca.2018.04.018.

Ballentine CJ, Marty B, Sherwood Lollar B, Cassidy M. Neon isotopes constrain convection and volatile origin in the Earth's mantle. Nature 2005;433:33–8. doi:10.1038/nature03182.

Banks PM, Kockarts G. Aeronomy. Academic Press, 1973.

Baraffe I, Chabrier G, Allard F, Hauschildt PH. Evolutionary models for solar metallicity low-mass stars: mass-magnitude relationships and color-magnitude diagrams. Astron Astrophys 1998;337:403–12. arXiv:astro-ph/9805009.

Baraffe I, Homeier D, Allard F, Chabrier G. New evolutionary models for pre- main sequence and main sequence low-mass stars down to the hydrogen-burning limit. Astron Astrophys 2015;577:A42. doi:10.1051/0004-6361/201425481. arXiv:1503.04107.

Basilevsky AT. Venera 8 landing site geology revisited. J. Geophys. Res. 1997;102:9257–62. doi:10.1029/97JE00413.

Benedikt M, Scherf M, Lammer H, Marcq E, Odert P, Leitzinger M, Erkaev N. Escape of rock-forming volatile elements and noble gases from planetary embryos. Icarus 2019;under revision.

Benz W, Asphaug E. Catastrophic Disruptions Revisited. Icarus 1999;142:5–20. doi:10.1006/icar.1999.6204. arXiv:astro-ph/9907117.

Birnstiel T, Fang M, Johansen A. Dust Evolution and the Formation of Planetes- imals. Space Sci. Rev. 2016;205:41–75. doi:10.1007/s11214-016-0256-1. arXiv:1604.02952.

Bollard J, Connelly JN, Whitehouse MJ, Pringle EA, Bonal L, Jørgensen JK, Nord- lund Å, Moynier F, Bizzarro M. Early formation of planetary building blocks inferred from Pb isotopic ages of chondrules. Science Advances 2017;3:e1700407. doi:10.1126/sciadv.1700407. arXiv:1708.02631.

Bonsor A, Leinhardt ZM, Carter PJ, Elliott T, Walter MJ, Stewart ST. A colli- sional origin to Earth's non-chondritic composition? Icarus 2015;247:291–300. doi:10.1016/j.icarus.2014.10.019. arXiv:1410.3421.

Bouhifd MA, Jephcoat AP. Convergence of Ni and Co metal-silicate partition co-efficients in the deep magma-ocean and coupled silicon-oxygen solubility in iron melts at high pressures. Earth and Planetary Science Letters 2011;307:341–8. doi:10.1016/j.epsl.2011.05.006.

Budde G, Burkhardt C, Kleine T. Molybdenum isotopic evidence for the late accretion of outer Solar System material to Earth. Nature Astronomy 2019;doi:10.1038/s41550-019-0779-y.

Burger C, Maindl TI, Schäfer CM. Transfer, loss and physical processing of water in hit-and-run collisions of planetary embryos. Celestial Mechanics and Dynamical Astronomy 2018;130:2. doi:10.1007/s10569-017-9795-3. arXiv:1710.03669.

Burger C, Schäfer CM. Applicability and limits of simple hydrodynamic scal- ing for collisions of water-rich bodies in different mass regimes. Proceedings of the First Greek-Austrian Workshop on Extrasolar Planetary Systems 2017;:63–81arXiv:1704.06075.

Caffee MW, Nishiizumi K. Exposure history of separated phases from the Kapoeta meteorite. Meteoritics and Planetary Science 2001;36:429–37. doi:10.1111/j.1945-5100.2001.tb01884.x.

Canup RM. Forming a Moon with an Earth-like Composition via a Giant Impact. Science 2012;338:1052. doi:10.1126/science.1226073.

Carroll D, Draper R, Brooker R, Kelley S. Noble gas solubilities in melts and crystals. In:Noble Gas Geochemistry and Cosmochemistry (ed J Matsuda) 1994;:325–41.

Carter PJ, Leinhardt ZM, Elliott T, Walter MJ, Stewart ST. Composi- tional Evolution during Rocky Protoplanet Accretion. ApJ 2015;813:72. doi:10.1088/0004-637X/813/1/72. arXiv:1509.07504.

Cassata WS. Meteorite constraints on Martian atmospheric loss and paleoclimate. Earth and Planetary Science Letters 2017;479:322–9. doi:10.1016/j.epsl.2017.09.034.

Catling DC, Kasting JF. Atmospheric Evolution on Inhabited and Lifeless Worlds. Cambridge University Press, 2017.

Christian DJ, Athioudakis M. High-Resolution Optical Observations of Extreme-Ultraviolet-selected Active Late-type Stars. Astrophys J 2002;123:2796–805. doi:10.1086/339702.

Conrad PG, Malespin CA, Franz HB, Pepin RO, Trainer MG, Schwenzer SP, Atreya SK, Freissinet C, Jones JH, Manning H, Owen T, Pavlov AA, Wiens RC, Wong MH, Mahaffy PR. In situ measurement of atmospheric krypton and xenon on Mars with Mars Science Laboratory. Earth and Planetary Science Letters 2016;454:1–9. doi:10.1016/j.epsl.2016.08.028.

Costa A, Caricchi L, Bagdassarov N. A model for the rheology of particle-bearing suspensions and partially molten rocks. Geochemistry, Geophysics, Geosystems 2009;10:Q03010. doi:10.1029/2008GC002138.

Crumpler LS, Aubele JC, Senske DA, Keddie ST, Magee KP, Head JW. Volcanoes and Centers of Volcanism on Venus. In: Bougher SW, Hunten DM, Phillips RJ, editors. Venus II: Geology, Geophysics, Atmosphere, and Solar Wind Environment. 1997. p. 697.

Cubillos P, Erkaev NV, Juvan I, Fossati L, Johnstone CP, Lammer H, Lendl M, Odert

P, Kislyakova KG. An overabundance of low-density Neptune-like planets. MNRAS 2017;466:1868–79. doi:10.1093/mnras/stw3103. arXiv:1611.09236.

Dauphas N. The isotopic nature of the Earth's accreting material through time. Nature 2017;541:521–4. doi:10.1038/nature20830.

Dauphas N, Chen JH, Zhang J, Papanastassiou DA, Davis AM, Travaglio C. Calcium-48 isotopic anomalies in bulk chondrites and achondrites: Evidence for a uniform isotopic reservoir in the inner protoplanetary disk. Earth and Planetary Science Letters 2014;407:96–108. doi:10.1016/j.epsl.2014.09.015.

Dauphas N, Schauble EA. Mass Fractionation Laws, Mass-Independent Effects, and Isotopic Anomalies. Annual Review of Earth and Planetary Sciences 2016;44:709–83. doi:10.1146/annurev-earth-060115-012157.

Davis AM, Holland HD, Turekian KK. Meteorites, Comets and Planets: Treatise on Geochemistry, Volume 1. Elsevier B, 2005.

Donahue TM. Fractionation of noble gases by thermal escape from accreting planetesimals. Icarus 1986;66:195–210. doi:10.1016/0019-1035(86)90151-X.

Dorfi EA, Pikall H, Stökl A, Gautschy A. Towards a more consistent discretization scheme for adaptive implicit RHD computations. Computer Physics Communications 2006;174:771–82. doi:10.1016/j.cpc.2005.12.012.

Erkaev NV, Kulikov YN, Lammer H, Selsis F, Langmayr D, Jaritz GF, Biernat HK. Roche lobe effects on the atmospheric loss from "Hot Jupiters". A&A 2007;472:329–34. doi:10.1051/0004-6361:20066929. arXiv:astro-ph/0612729.

Erkaev NV, Lammer H, Elkins-Tanton LT, Stökl A, Odert P, Marcq E, Dorfi EA, Kislyakova KG, Kulikov YN, Leitzinger M, Güdel M. Escape of the martian protoatmosphere and initial water inventory. Planet Space Sci 2014;98:106–19. doi:10.1016/j.pss.2013.09.008. arXiv:1308.0190.

Erkaev NV, Lammer H, Odert P, Kislyakova KG, Johnstone CP, Güdel M, Khodachenko ML. EUV-driven mass-loss of protoplanetary cores with hydrogen-dominated atmospheres: the influences of ionization and orbital distance. MNRAS 2016;460:1300–9. doi:10.1093/mnras/stw935. arXiv:1601.00452.

Erkaev NV, Lammer H, Odert P, Kulikov YN, Kislyakova KG. Extreme hydrodynamic atmospheric loss near the critical thermal escape regime. MNRAS 2015;448:1916–21. doi:10.1093/mnras/stv130. arXiv:1506.06592.

Evans II NJ, Dunham MM, Jørgensen JK, Enoch ML, Merín B, van Dishoeck EF, Alcalá JM, Myers PC, Stapelfeldt KR, Huard TL, Allen LE, Harvey PM, van Kempen T, Blake GA, Koerner DW, Mundy LG, Padgett DL, Sargent AI. The Spitzer c2d Legacy Results: Star-Formation Rates and Efficiencies; Evolution and Lifetimes. ApJS 2009;181:321–50. doi:10.1088/0067-0049/181/2/321. arXiv:0811.1059.

Fegley Jr. B, Jacobson NS, Williams KB, Plane JMC, Schaefer L, Lodders K. Solubility of Rock in Steam Atmospheres of Planets. ApJ 2016;824:103. doi:10.3847/0004-637X/824/2/103. arXiv:1602.00658.

Fiquet G, Auzende AL, Siebert J, Corgne A, Bureau H, Ozawa H, Garbarino G. Melting of Peridotite to 140 Gigapascals. Science 2010;329:1516. doi:10.1126/science.1192448.

Fischer-Gödde M, Kleine T. Ruthenium isotopic evidence for an inner Solar System origin of the late veneer. Nature 2017;541:525–7. doi:10.1038/nature21045.

Fossati L, Erkaev NV, Lammer H, Cubillos PE, Odert P, Juvan I, Kislyakova KG, Lendl M, Kubyshkina D, Bauer SJ. Aeronomical constraints to the minimum mass and maximum radius of hot low-mass planets. Astron Astrophys 2017;598:A90. doi:10.1051/0004-6361/201629716. arXiv:1612.05624.

Fox JL, Hać A. The $^{15}N/^{14}N$ isotope fractionation in dissociative recombination of N_2^+. J. Geophys. Res. 1997;102:9191–204. doi:10.1029/97JE00086.

Füri E, Marty B. Nitrogen isotope variations in the Solar System. Nature Geoscience 2015;8:515–22. doi:10.1038/ngeo2451.

Gale A, Dalton CA, Langmuir CH, Su Y, Schilling JG. The mean composition of ocean ridge basalts. Geochemistry, Geophysics, Geosystems 2013;14:489–518. doi:10.1029/2012GC004334.

Genda H, Abe Y. Survival of a proto-atmosphere through the stage of giant impacts: the mechanical aspects. Icarus 2003;164:149–62. doi:10.1016/S0019-1035(03)00101-5.

Gillmann C, Chassefière E, Lognonné P. A consistent picture of early hydrodynamic escape of Venus atmosphere explaining present Ne and Ar isotopic ratios and low oxygen atmospheric content. Earth and Planetary Science Letters 2009;286:503–13. doi:10.1016/j.epsl.2009.07.016.

Göbel R, Ott U, Begemann F. On trapped noble gases in ureilites. J. Geophys. Res. 1978;83:855–67. doi:10.1029/JB083iB02p00855.

H. Tillotson J. Metallic Equations of State for Hypervelocity Impact. volume GA-3216. PN (1962), 1962.

Haghighipour N, Maindl TI, Schaefer CM, Wandel OJ. Triggering the Activation of Main Belt Comets: The Effect of Porosity. ArXiv e-prints 2018;arXiv:1801.08247.

Halliday A, Rehkämper M, Lee DC, Yi W. Early evolution of the Earth and Moon: new constraints from Hf-W isotope geochemistry. Earth and Planetary Science Letters 1996;142:75–89. doi:10.1016/0012-821X(96)00096-9.

Halliday AN. HF-W Chronometry and Inner Solar System Accretion Rates. Space Sci. Rev. 2000;92:355–70. doi:10.1023/A:1005280220751.

Hamano K, Abe Y, Genda H. Emergence of two types of terrestrial planet on solidification of magma ocean. Nature 2013;497:607–10. doi:10.1038/nature12163.

Harper CL, Wiesmann H, Nyquist LE. ^{135}Cs-^{135}Ba: Very high precision isotopic investigations and a new cosmochronometric constraint on the astrophysical site of the origin of the solar system. Meteoritics 1991;26:341.

Hayashi C. Formation of the planets. In: Sugimoto D, Lamb DQ, Schramm DN, editors. Fundamental Problems in the Theory of Stellar Evolution. volume 93 of *IAU Symposium*; 1981. p. 113–26.

Heber VS, Baur H, Bochsler P, McKeegan KD, Neugebauer M, Reisenfeld DB, Wieler R, Wiens RC. Isotopic Mass Fractionation of Solar Wind: Evidence from Fast and Slow Solar Wind Collected by the Genesis mission. ApJ 2012;759:121. doi:10.1088/0004-637X/759/2/121.

Hébrard E, Marty B. Coupled noble gas-hydrocarbon evolution of the early Earth atmosphere upon solar UV irradiation. Earth and Planetary Science Letters 2014;385:40–8. doi:10.1016/j.epsl.2013.10.022.

Herzberg C, Raterron P, Zhang J. New experimental observations on the anhydrous solidus for peridotite KLB-1. Geochemistry, Geophysics, Geosystems 2000;1:1051–14. doi:10.1029/2000GC000089.

Herzog GF, Moynier F, Albarède F, Berezhnoy AA. Isotopic and elemen- tal abundances of copper and zinc in lunar samples, Zagami, Pele's hairs, and a terrestrial basalt. Geochimica et Cosmochimica Acta 2009;73:5884–904. doi:10.1016/j.gca.2009.05.067.

Hoffman JH, Hodges RR, Donahue TM, McElroy MM. Composition of the Venus lower atmosphere from the Pioneer Venus mass spectrometer. J Geophys Res 1980;85:7882–90. doi:10.1029/JA085iA13p07882.

Hunten DM, Pepin RO, Walker JCG. Mass fractionation in hydrodynamic escape. Icarus 1987;69:532–49. doi:10.1016/0019-1035(87)90022-4.

Hutchins KS, Jakosky BM. Evolution of Martian atmospheric argon: Im- plications for sources of volatiles. J. Geophys. Res. 1996;101:14933–50. doi:10.1029/96JE00860.

Ikoma M, Genda H. Constraints on the Mass of a Habitable Planet with Wa- ter of Nebular Origin. Astrophys J 2006;648:696–706. doi:10.1086/505780. arXiv:astro-ph/0606117.

Inamdar NK, Schlichting HE. Stealing the Gas: Giant Impacts and the Large Diversity in Exoplanet Densities. Astrophys Jl 2016;817:L13. doi:10.3847/2041-8205/817/2/L13. arXiv:1510.02090.

Istomin VG, Grechnev KV, Kochnev VA. Mass spectrometer measurements of the composition of the lower atmosphere of Venus. In: Deepak A, editor. Space Research XX. 1980. p. 215–8.

Istomin VG, Grechnev KV, Kochnev VA. Venera 13 and 14 - Mass spectroscopy of the atmosphere. Kosmicheskie Issledovaniia 1983;21:410–20.

Jakosky BM, Pepin RO, Johnson RE, Fox JL. Mars atmospheric loss and isotopic fractionation by solar-wind-induced sputtering and photochemical escape. Icarus 1994;111:271–88. doi:10.1006/icar.1994.1145.

Jakosky BM, Slipski M, Benna M, Mahaffy P, Elrod M, Yelle R, Stone S, Alsaeed N. Mars' atmospheric history derived from upper-atmosphere measurements of $^{38}Ar/^{36}Ar$. Science 2017;355:1408–10. doi:10.1126/science.aai7721.

Jaupart E, Charnoz S, Moreira M. Primordial atmosphere incorporation in planetary embryos and the origin of Neon in terrestrial planets. Icarus 2017;293:199 – 205. doi:https://doi.org/10.1016/j.icarus.2017.04.022.

Javoy M, Kaminski E, Guyot F, Andrault D, Sanloup C, Moreira M, Labrosse S, Jambon A, Agrinier P, Davaille A, Jaupart C. The chemical composition of the Earth: Enstatite chondrite models. Earth and Planetary Science Letters 2010;293:259–68. doi:10.1016/j.epsl.2010.02.033.

Jellinek AM, Jackson MG. Connections between the bulk composition, geo- dynamics and habitability of Earth. Nature Geoscience 2015;8:587–93. doi:10.1038/ngeo2488.

Johansen A, Mac Low MM, Lacerda P, Bizzarro M. Growth of asteroids, plane- tary embryos, and Kuiper belt objects by chondrule accretion. Science Advances 2015;1:1500109. doi:10.1126/sciadv.1500109. arXiv:1503.07347.

Johnstone CP, Güdel M, Stökl A, Lammer H, Tu L, Kislyakova KG, Lüftinger T, Odert P, Erkaev NV, Dorfi EA. The Evolution of Stellar Rotation and the Hydrogen Atmospheres of Habitable-zone Terrestrial Planets. Astrophys Jl 2015;815:L12. doi:10.1088/2041-8205/815/1/L12. arXiv:1511.03647.

Karki BB, Stixrude LP. Viscosity of $MgSiO_3$ Liquid at Earth's Mantle Con- ditions: Implications for an Early Magma Ocean. Science 2010;328:740. doi:10.1126/science.1188327.

Kleine T, Münker C, Mezger K, Palme H. Rapid accretion and early core formation on asteroids and the terrestrial planets from Hf-W chronometry. Nature 2002;418:952–5. doi:10.1038/nature00982.

Kleine T, Walker RJ. Tungsten Isotopes in Planets. Annual Review of Earth and Plane- tary Sciences 2017;45:389–417. doi:10.1146/annurev-earth-063016-020037.

Koskinen TT, Yelle RV, Harris MJ, Lavvas P. The escape of heavy atoms from the iono- sphere of HD209458b. II. Interpretation of the observations. Icarus 2013;226:1695–708. doi:10.1016/j.icarus.2012.09.026. arXiv:1210.1543.

Kubyshkina D, Fossati L, Erkaev NV, Johnstone CP, Cubillos PE, Kislyakova KG, Lammer H, Lendl M, Odert P. Grid of upper atmosphere models for 1-40 M planets: application to CoRoT-7 b and HD 219134 b,c. A&A 2018a;619:A151. doi:10.1051/0004-6361/201833737. arXiv:1809.06645.

Kubyshkina D, Lendl M, Fossati L, Cubillos P, Lammer H, Erkaev N, Johnstone C. Young planets under extreme uv irradiation. i. upper atmosphere modelling of the young exoplanet k2-33b. Astron Astrophys 2018b;:in press.

Lambrechts M, Johansen A. Rapid growth of gas-giant cores by pebble accretion. A&A 2012;544:A32. doi:10.1051/0004-6361/201219127. arXiv:1205.3030.

Lammer H, Erkaev NV, Fossati L, Juvan I, Odert P, Cubillos PE, Guenther E, Kislyakova KG, Johnstone CP, Lüftinger T, Güdel M. Identifying the 'true' radius of the hot sub-Neptune CoRoT-24b by mass-loss modelling. MNRAS 2016;461:L62–6. doi:10.1093/mnrasl/slw095. arXiv:1605.03595.

Lammer H, Spross L, Grenfell L, Scherf M, Fossati L, Lendl M, Cubillos P. The role of N_2 as a geo-biosignatiure for the detection and characterization of Earth-like habitats. Astrobiology 2019;in press.

Lammer H, Stökl A, Erkaev NV, Dorfi EA, Odert P, Güdel M, Kulikov YN, Kislyakova KG, Leitzinger M. Origin and loss of nebula-captured hydrogen en- velopes from 'sub'- to 'super-Earths' in the habitable zone of Sun-like stars. MNRAS 2014;439:3225–38. doi:10.1093/mnras/stu085. arXiv:1401.2765.

Lammer H, Zerkle AL, Gebauer S, Tosi N, Noack L, Scherf M, Pilat-Lohinger E, Güdel M, Grenfell JL, Godolt M, Nikolaou A. Origin and evolution of the atmospheres of early Venus, Earth and Mars. A&A Rev. 2018;26:2. doi:10.1007/s00159-018-0108-y.

Lebrun T, Massol H, ChassefièRe E, Davaille A, Marcq E, Sarda P, Leblanc F,

Brandeis G. Thermal evolution of an early magma ocean in interaction with the atmosphere. Journal of Geophysical Research (Planets) 2013;118:1155–76. doi:10.1002/jgre.20068.

Levison HF, Kretke KA, Walsh KJ, Bottke WF. Growing the terrestrial planets from the gradual accumulation of sub-meter sized objects. Proceedings of the Na- tional Academy of Science 2015;112:14180–5. doi:10.1073/pnas.1513364112. arXiv:1510.02095.

Lichtenegger HIM, Kislyakova KG, Odert P, Erkaev NV, Lammer H, Gröller H, Johnstone CP, Elkins-Tanton L, Tu L, Güdel M, Holmström M. Solar XUV and ENA-driven water loss from early Venus' steam atmosphere. Journal of Geophysical Research (Space Physics) 2016;121:4718–32. doi:10.1002/2015JA022226.

Lindsay FN, Herzog GF, Park J, Delaney JS, Turrin BD, Swisher CC. $^{40}Ar/^{39}Ar$ dating of microgram feldspar grains from the paired feldspathic achon- drites GRA 06128 and 06129. Geochim Cosmochim Acta 2014;129:96–110. doi:10.1016/j.gca.2013.12.023.

Lodders K. Solar System Abundances and Condensation Temperatures of the Elements. Astrophys J 2003;591:1220–47. doi:10.1086/375492.

Lodders K, Palme H, Gail HP. Abundances of the Elements in the Solar System. Landolt Börnstein 2009;doi:10.1007/978-3-540-88055-4_34. arXiv:0901.1149.

Lyubetskaya T, Korenaga J. Chemical composition of Earth's primitive mantle and its variance: 1. Method and results. Journal of Geophysical Research (Solid Earth) 2007;112:B03211. doi:10.1029/2005JB004223.

Maindl TI, Dvorak R, Schäfer C, Speith R. Fragmentation of colliding planetesimals with water content. In: Complex Planetary Systems, Proceedings of the Inter-

national Astronomical Union. volume 310 of *IAU Symposium*; 2014. p. 138–41. doi:10.1017/S1743921314008059. arXiv:1409.2298.

Mamajek EE. Initial Conditions of Planet Formation: Lifetimes of Primordial Disks. In: Usuda T, Tamura M, Ishii M, editors. American Institute of Physics Conference Series. volume 1158 of *American Institute of Physics Conference Series*; 2009. p. 3–10. doi:10.1063/1.3215910. arXiv:0906.5011.

Marcq E. A simple 1-D radiative-convective atmospheric model designed for integration into coupled models of magma ocean planets. Journal of Geophysical Research (Planets) 2012;117:E01001. doi:10.1029/2011JE003912.

Marcq E, Salvador A, Massol H, Davaille A. Thermal radiation of magma ocean planets using a 1-D radiative-convective model of H_2O-CO_2 atmospheres. Journal of Geophysical Research (Planets) 2017;122:1539–53. doi:10.1002/2016JE005224.

Marty B. The origins and concentrations of water, carbon, nitrogen and no- ble gases on Earth. Earth and Planetary Science Letters 2012;313:56–66. doi:10.1016/j.epsl.2011.10.040. arXiv:1405.6336.

Marty B, Allé P. Neon and argon isotopic constraints on earth-atmosphere evolution. In: Matsuda J, editor. Noble Gas Geochemistry and Cosmochemistry. TERRAPUB; 1994. p. 191–204.

Mazor E, Heymann D, Anders E. Noble gases in carbona- ceous chondrites. Geochim. Cosmochim. Acta 1970;34:781–824. doi:10.1016/0016-7037(70)90031-1.

McSween HY. Planetary science: A chunk of ancient Mars. Nature 2013;503:473–4. doi:10.1038/nature12836.

Melosh HJ. Impact cratering: A geologic process. Oxford University Press, 1989.

Meshik A, Hohenberg C, Pravdivtseva O, Burnett D. Heavy noble gases in solar wind delivered by Genesis mission. Geochim Cosmochim Acta 2014;127:326–47. doi:10.1016/j.gca.2013.11.030.

Mikhail S, Sverjensky DA. Nitrogen speciation in upper mantle fluids and the origin of Earth's nitrogen-rich atmosphere. Nature Geoscience 2014;7:816–9. doi:10.1038/ngeo2271.

Miller S, Stallard T, Tennyson J, Melin H. Cooling by H3+ Emission. Journal of Physical Chemistry A 2013;117:9770–7. doi:10.1021/jp312468b.

Mizuno H, Nakazawa K, Hayashi C. Dissolution of the primordial rare gases into the molten earth's material. Earth and Planetary Science Letters 1980;50:202–10. doi:10.1016/0012-821X(80)90131-4.

Montmerle T, Augereau JC, Chaussidon M, Gounelle M, Marty B, Morbidelli A. From Suns to Life: A Chronological Approach to the History of Life on Earth 3. Solar System Formation and Early Evolution: the First 100 Million Years. Earth Moon and Planets 2006;98:39–95. doi:10.1007/s11038-006-9087-5.

Morbidelli A. Calcium signals in planetary embryos. Nature 2018;555:451–2. doi:10.1038/d41586-018-03144-1.

Moreira M, Charnoz S. The origin of the neon isotopes in chondrites and on Earth. Earth and Planetary Science Letters 2016;433:249–56. doi:10.1016/j.epsl.2015.11.002.

Moreira M, Kunz J, Allegre C. Rare Gas Systematics in Popping Rock: Iso- topic and Elemental Compositions in the Upper Mantle. Science 1998;279:1178. doi:10.1126/science.279.5354.1178.

Moreira MA, Kurz MD. Noble Gases as Tracers of Mantle Processes and Magmatic Degassing; Berlin, Heidelberg: Springer Berlin Heidel-

berg. p. 371–91. URL: https://doi.org/10.1007/978-3-642-28836-4_12. doi:10.1007/978-3-642-28836-4_12.

Mukhopadhyay S. Early differentiation and volatile accretion recorded in deep-mantle neon and xenon. Nature 2012;486:101–4. doi:10.1038/nature11141.

Murthy VR, van Westrenen W, Fei Y. Experimental evidence that potassium is a substantial radioactive heat source in planetary cores. Nature 2003;423:163–5. doi:10.1038/nature01560.

Newsom HE, Sims KWW, Noll PD, Jaeger WL, Maehr SA, Beserra TB. The depletion of tungsten in the bulk silicate earth: Constraints on core formation. Geochim. Cosmochim. Acta 1996;60:1155–69. doi:10.1016/0016-7037(96)00029-4.

Nimmo F. Thermal and Compositional Evolution of the Core. Treatise on Geophysics 2007;9:201–9. doi:10.1016/B978-044452748-6.00147-4.

O'Brien DP, Morbidelli A, Levison HF. Terrestrial planet formation with strong dynamical friction. Icarus 2006;184:39–58. doi:10.1016/j.icarus.2006.04.005.

Odert P, Lammer H, Erkaev NV, Nikolaou A, Lichtenegger HIM, Johnstone CP, Kislyakova KG, Leitzinger M, Tosi N. Escape and fractionation of volatiles and noble gases from Mars-sized planetary embryos and growing protoplanets. Icarus 2018;307:327–46. doi:10.1016/j.icarus.2017.10.031. arXiv:1706.06988.

O'Neill HSC, Palme H. Collisional erosion and the non-chondritic composition of the terrestrial planets. Philosophical Transactions of the Royal Society of London Series A 2008;366:4205–38. doi:10.1098/rsta.2008.0111.

Owen JE, Wu Y. Atmospheres of low-mass planets: The "boil-off". The Astrophysical Journal 2016;817(2):107. URL: http://stacks.iop.org/0004-637X/817/i=2/a=107.

Ozima M, Podosek FA. Noble Gas Geochemistry. Cambridge University Press, 1983.

Pahlevan K, Schaefer L, Hirschmann MM. Hydrogen isotopic evidence for early oxidation of silicate Earth. Earth and Planetary Science Letters 2019;submitted.

Palma RL, Becker RH, Pepin RO, Schlutter DJ. Irradiation records in regolith ma- terials, II: Solar wind and solar energetic particle components in helium, neon, and argon extracted from single lunar mineral grains and from the Kapoeta howardite by stepwise pulse heating. Geochim Cosmochim Acta 2002;66:2929– 58. doi:10.1016/S0016-7037(02)00853-0.

Paniello RC, Day JMD, Moynier F. Zinc isotopic evidence for the origin of the Moon. Nature 2012;490:376–9. doi:10.1038/nature11507.

Patzer A, Schultz L. Noble gases in enstatite chondrites I: Exposure ages, pair- ing, and weathering effects. Meteoritics and Planetary Science 2001;36:947–61. doi:10.1111/j.1945-5100.2001.tb01932.x.

Patzer A, Schultz L. Noble gases in enstatite chondrites II: The trapped component. Meteoritics and Planetary Science 2002;37:601–12. doi:10.1111/j.1945-5100.2002.tb00841.x.

Pepin RO. On the origin and early evolution of terrestrial planet atmospheres and meteoritic volatiles. Icarus 1991;92:2–79. doi:10.1016/0019-1035(91)90036-S.

Pepin RO. Evolution of Earth's Noble Gases: Consequences of Assum- ing Hydrodynamic Loss Driven by Giant Impact. Icarus 1997;126:148–56. doi:10.1006/icar.1996.5639.

Pepin RO. Atmospheres on the terrestrial planets: Clues to ori- gin and evolution. Earth and Planetary Science Letters 2006;252:1–14. doi:10.1016/j.epsl.2006.09.014.

Pepin RO, Becker RH, Schlutter DJ. Irradiation records in regolith ma- terials, I: Isotopic compositions of solar-wind neon and argon in sin- gle lunar mineral grains. Geochim. Cosmochim. Acta 1999;63:2145–62. doi:10.1016/S0016-7037(99)00002-2.

Péron S, Moreira M, Agranier A. Origin of Light Noble Gases (He, Ne, and Ar) on Earth: A Review. Geochemistry, Geophysics, Geosystems 2018;19(4):979–96. doi:10.1002/2017GC007388.

Péron S, Moreira M, Colin A, Arbaret L, Putlitz B, Kurz MD. Neon isotopic composition of the mantle constrained by single vesicle analyses. Earth and Planetary Science Letters 2016;449:145–54. doi:10.1016/j.epsl.2016.05.052.

Porcelli D, Woolum D, Cassen P. Deep Earth rare gases: initial inventories, capture from the solar nebula, and losses during Moon formation. Earth and Planetary Science Letters 2001;193:237–51. doi:10.1016/S0012-821X(01)00493-9.

Rai N, Downes H, Smith CL. Bulk Compositions of the Ureilite Parent Body and Vesta: Constraints from Oxygen Isotopes. In: Lunar and Planetary Science Conference. volume 47 of *Lunar and Planetary Inst. Technical Report*; 2016. p. 1702.

Raquin A, Moreira M. Atmospheric $^{38}Ar/^{36}Ar$ in the mantle: Implications for the nature of the terrestrial parent bodies. Earth and Planetary Science Letters 2009;287:551–8. doi:10.1016/j.epsl.2009.09.003.

Rudge JF, Kleine T, Bourdon B. Broad bounds on Earth's accretion and core for- mation constrained by geochemical models. Nature Geoscience 2010;3:439–43. doi:10.1038/ngeo872.

Salvador A, Massol H, Davaille A, Marcq E, Sarda P, Chassefière E. The rela- tive influence of H_2O and CO_2 on the primitive surface conditions and evolution

of rocky planets. Journal of Geophysical Research (Planets) 2017;122:1458–86. doi:10.1002/2017JE005286.

Sasaki S, Nakazawa K. Did a primary solar-type atmosphere exist around the proto-earth? Icarus 1990;85:21–42. doi:10.1016/0019-1035(90)90101-E.

Schaefer L, Fegley B. Chemistry of atmospheres formed during accre- tion of the Earth and other terrestrial planets. Icarus 2010;208:438–48. doi:10.1016/j.icarus.2010.01.026. arXiv:0909.4050.

Schäfer C, Riecker S, Maindl TI, Speith R, Scherrer S, Kley W. A smooth par- ticle hydrodynamics code to model collisions between solid, self-gravitating ob- jects. Astron Astrophys 2016;590:A19. doi:10.1051/0004-6361/201528060. arXiv:1604.03290.

Schäfer CM, Scherrer S, Buchwald R, Maindl TI, Speith R, Kley W. Numerical simulations of regolith sampling processes. Planet Space Sci 2017;141:35–44. doi:10.1016/j.pss.2017.04.015. arXiv:1705.00893.

Schiller M, Bizzarro M, Fernandes VA. Isotopic evolution of the protoplanetary disk and the building blocks of Earth and the Moon. Nature 2018;555:507–10. doi:10.1038/nature25990.

Schlichting HE, Sari R, Yalinewich A. Atmospheric mass loss during planet formation: The importance of planetesimal impacts. Icarus 2015;247:81–94. doi:10.1016/j.icarus.2014.09.053. arXiv:1406.6435.

Sekiya M, Nakazawa K, Hayashi C. Dissipation of the rare gases contained in the primordial earth's atmosphere. Earth and Planetary Science Letters 1980;50:197– 201. doi:10.1016/0012-821X(80)90130-2.

Shang-Fei L, Yasunori H, Lin DNC, Asphaug E. Giant impact: An efficient mechanism

for the devolatilization of super-earths. The Astrophysical Journal 2015;812(2):164. URL: http://stacks.iop.org/0004-637X/812/i=2/a=164.

Shematovich VI, Bisikalo DV, Barabash S, Stenberg G. Monte Carlo study of interaction between solar wind plasma and Venusian upper atmosphere. Solar System Research 2014;48:317–23. doi:10.1134/S0038094614050049.

Shuvalov V. Atmospheric erosion induced by oblique impacts. Meteoritics and Planetary Science 2009;44:1095–105. doi:10.1111/j.1945-5100.2009.tb01209.x.

Siess L, Dufour E, Forestini M. An internet server for pre-main sequence tracks of low- and intermediate-mass stars. Astron Astrophys 2000;358:593–9. arXiv:astro-ph/0003477.

Solomatov V. Magma Oceans and Primordial Mantle Differentiation; Elsevier; vol- ume 9. p. 91–119. doi:10.1016/B978-044452748-6.00141-3.

Sossi PA, Klemme S, O'Neill HSC, Berndt J, Moynier F. Evaporation of moder- ately volatile elements from silicate melts: experiments and theory. Geochim. Cos- mochim. Acta 2019;260:204–31. doi:10.1016/j.gca.2019.06.021.

Stökl A. A two-column formalism for time-dependent modelling of stellar con- vection. I. Description of the method. Astron Astrophys 2008;490:1181–95. doi:10.1051/0004-6361:200810144. arXiv:0809.0862.

Stökl A, Dorfi E, Lammer H. Hydrodynamic simulations of captured pro- toatmospheres around Earth-like planets. Astron Astrophys 2015;576:A87. doi:10.1051/0004-6361/201423638. arXiv:1505.06859.

Stökl A, Dorfi EA. 2-dimensional implicit hydrodynamics on adaptive grids. Computer Physics Communications 2007;177:815–31. doi:10.1016/j.cpc.2007.06.012.

Stökl A, Dorfi EA, Johnstone CP, Lammer H. Dynamical Accretion of Primordial Atmospheres around Planets with Masses between 0.1 and 5 M in the Habitable Zone. Astrophys J 2016;825:86. doi:10.3847/0004-637X/825/2/86.

Surkov IA, Kirnozov FF, Glazov VN, Dunchenko AG, Tatsii LP. Content of natural radioactive elements in Venusian soils from Venera 9 and 10 data. Kosmicheskie Issledovaniia 1976;14:704–9.

Taylor SR. Chondritic Earth Model. Nature 1964;202:281–2. doi:10.1038/202281a0.

Tognelli E, Prada Moroni PG, Degl'Innocenti S. The Pisa pre-main sequence tracks and isochrones. A database covering a wide range of Z, Y, mass, and age val- ues. Astron Astrophys 2011;533:A109. doi:10.1051/0004-6361/200913913. arXiv:1107.2318.

Trieloff M, Kunz J, Clague DA, Harrison D, Allègre CJ. The Nature of Pristine Noble Gases in Mantle Plumes. Science 2000;288:1036–9. doi:10.1126/science.288.5468.1036.

Trigo-Rodríguez JM. Nitrogen in Solar System Minor Bodies: Delivery Path- ways to Primeval Earth. In: Trigo-Rodriguez JM, Raulin F, Muller C, Nixon C, editors. The Early Evolution of the Atmospheres of Terrestrial Plan- ets. volume 35 of *Astrophysics and Space Science Proceedings*; 2013. p. 9. doi:10.1007/978-1-4614-5191-4_2.

Tu L, Johnstone CP, Güdel M, Lammer H. The extreme ultraviolet and X-ray Sun in Time: High-energy evolutionary tracks of a solar-like star. Astron Astrophys 2015;577:L3. doi:10.1051/0004-6361/201526146. arXiv:1504.04546.

Turcotte DL, Schubert G. Geodynamics, 2002.

Valencia D, O'Connell RJ, Sasselov D. Internal structure of massive terres-

trial planets. Icarus 2006;181:545–54. doi:10.1016/j.icarus.2005.11.021. arXiv:astro-ph/0511150.

Varas-Reus MI, König S, Yierpan A, Lorand JP, Schoenberg R. Selenium isotopes as tracers of a late volatile contribution to Earth from the outer Solar System. Nature Geoscience 2019;12:779–82. doi:10.1038/s41561-019-0414-7.

Vinogradov AP, Surkov YA, Kirnozov FF. The Content of Uranium, Thorium, and Potassium in the Rocks of Venus as Measured by Venera 8. Icarus 1973;20:253–9. doi:10.1016/0019-1035(73)90001-8.

Wang H, Weiss BP, Bai XN, Downey BG, Wang J, Wang J, Suavet C, Fu RR, Zucolotto ME. Lifetime of the solar nebula constrained by meteorite paleomagnetism. Science 2017;355:623–7. doi:10.1126/science.aaf5043.

Wang K, Jacobsen SB. An estimate of the Bulk Silicate Earth potassium isotopic composition based on MC-ICPMS measurements of basalts. Geochimica et Cosmochimica Acta 2016a;178:223–32. doi:10.1016/j.gca.2015.12.039.

Wang K, Jacobsen SB. Potassium isotopic evidence for a high-energy giant impact origin of the Moon. Nature 2016b;538:487–90. doi:10.1038/nature19341.

Wasson JT, Kallemeyn GW. Compositions of chondrites. Philosophical Transactions of the Royal Society of London Series A 1988;325:535–44. doi:10.1098/rsta.1988.0066.

Watson AJ, Donahue TM, Walker JCG. The dynamics of a rapidly escaping atmo- sphere - Applications to the evolution of earth and Venus. Icarus 1981;48:150–66. doi:10.1016/0019-1035(81)90101-9.

Williams CD, Mukhopadhyay S. Capture of nebular gases during Earth's accretion is preserved in deep-mantle neon. Nature 2019;565:78–81. doi:10.1038/s41586-018-0771-1.

Wood BJ, Halliday AN. Cooling of the Earth and core formation after the giant impact. Nature 2005;437:1345–8. doi:10.1038/nature04129.

Wordsworth RD. Atmospheric nitrogen evolution on Earth and Venus. Earth and Planetary Science Letters 2016;447:103–11. doi:10.1016/j.epsl.2016.04.002. arXiv:1605.07718.

Workman RK, Hart SR. Major and trace element composition of the depleted MORB mantle (DMM). Earth and Planetary Science Letters 2005;231:53–72. doi:10.1016/j.epsl.2004.12.005.

Yin Q, Jacobsen SB, Yamashita K, Blichert-Toft J, Télouk P, Albarède F. A short timescale for terrestrial planet formation from Hf-W chronometry of meteorites. Nature 2002;418:949–52. doi:10.1038/nature00995.

Yokochi R, Marty B. A determination of the neon isotopic composition of the deep mantle. Earth and Planetary Science Letters 2004;225:77–88. doi:10.1016/j.epsl.2004.06.010.

Young ED, Shahar A, Nimmo F, Schlichting HE, Schauble EA, Tang H, Labidi J. Near-equilibrium isotope fractionation during planetesimal evaporation. Icarus 2019;323:1–15. doi:10.1016/j.icarus.2019.01.012. arXiv:1909.05978.

Yu G, Jacobsen SB. Fast accretion of the Earth with a late Moon-forming gi- ant impact. Proceedings of the National Academy of Science 2011;108:17604–9. doi:10.1073/pnas.1108544108.

Zahnle K, Pollack JB, Kasting JF. Mass fractionation of noble gases in diffusion-limited hydrodynamic hydrogen escape. Icarus 1990;84:502–27. doi:10.1016/0019-1035(90)90050-J.

Zahnle KJ. Xenon Fractionation and Archean Hydrogen Escape. In: Lunar and

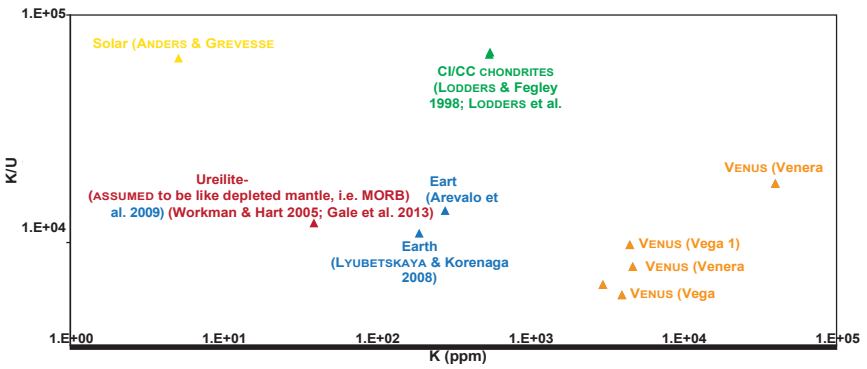

Figure 1: Average K/U ratio versus abundance of K (ppm) for different reservoirs. Present-day Earth and Venus show significantly lower K/U ratios than the volatile rich solar and chondritic reservoirs. Venus stands out with a high abundance of K, in particular as observed by Venera 8, whereas all other measurements on Venus are comparable in ratio and abundance. As can be clearly seen, the Venera 8 measurements, however, might not be representative for the bulk Venus composition (Basilevsky, 1997; Abdrakhimov and Basilevsky, 2002).

Planetary Science Conference. volume 46 of *Lunar and Planetary Inst. Technical Report*; 2015. p. 1549.

Zahnle KJ, Gacesa M, Catling DC. Strange messenger: A new history of hydro- gen on Earth, as told by Xenon. Geochim. Cosmochim. Acta 2019;244:56–85. doi:10.1016/j.gca.2018.09.017. arXiv:1809.06960.

Zahnle KJ, Kasting JF. Mass fractionation during transonic escape and im- plications for loss of water from Mars and Venus. Icarus 1986;68:462–80. doi:10.1016/0019-1035(86)90051-5.

Zhang J, Herzberg C. Melting experiments on anhydrous peridotite KLB-1 from 5.0 to 22.5 GPa. J Geophys Res 1994;99:17. doi:10.1029/94JB01406.

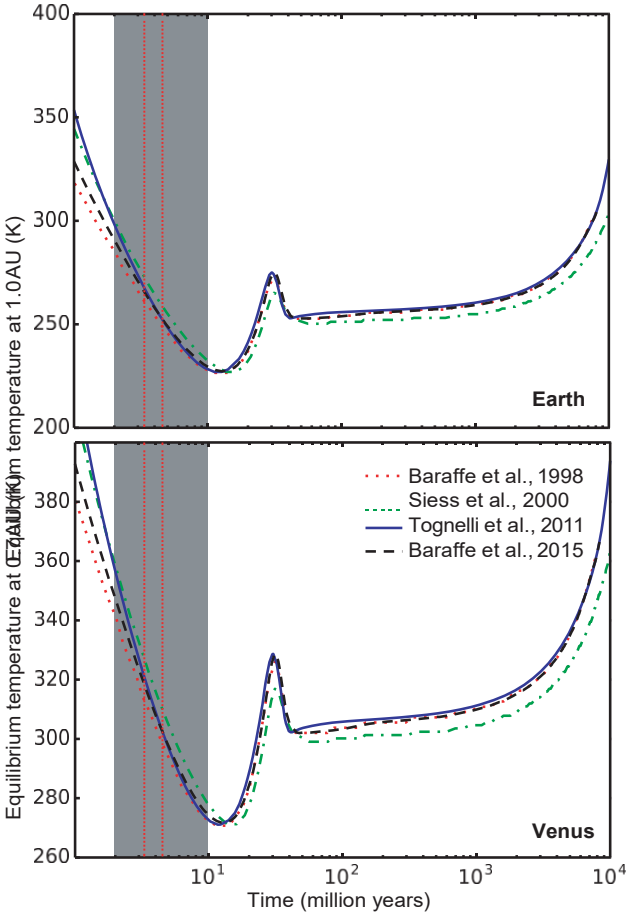

Figure 2: Equilibrium temperature evolution at the orbits of Venus and Earth. Modeled equilibrium temperature according to the evolution of the bolometric luminosity of the Sun at 1 AU (Earth) and 0.7 AU (Venus) as a function of time. The dark grey shaded area constrains the typical lifetime of circumstellar gas disks, while the two vertical dashed-lines correspond to the minimum and maximum lifetime the solar protoplanetary disk dated from the Pb isotope analysis of young chondrules Bollard et al. (2017).

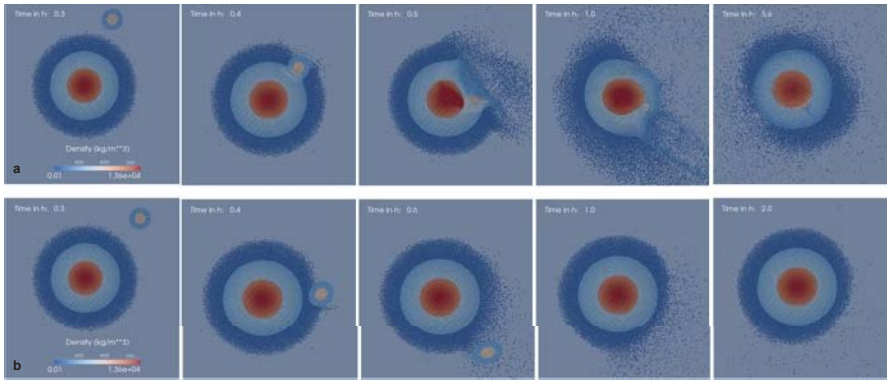

Figure 3: Collision snapshots. A protoplanet (0.6 $\times M_{Earth}$, covered in a 0.1 mass% H_2 atmosphere) is hit by a Moon-mass embryo, with an impact angle of 30° (a) and 75° (b). The density color-coding illustrates the internal core-mantle-atmosphere structure (bodies are cut into halves), i.e. atmosphere in dark blue, mantle in light blue, and iron core in red, respectively. The impact velocity is $2 \times v_{esc}$ in both scenarios.

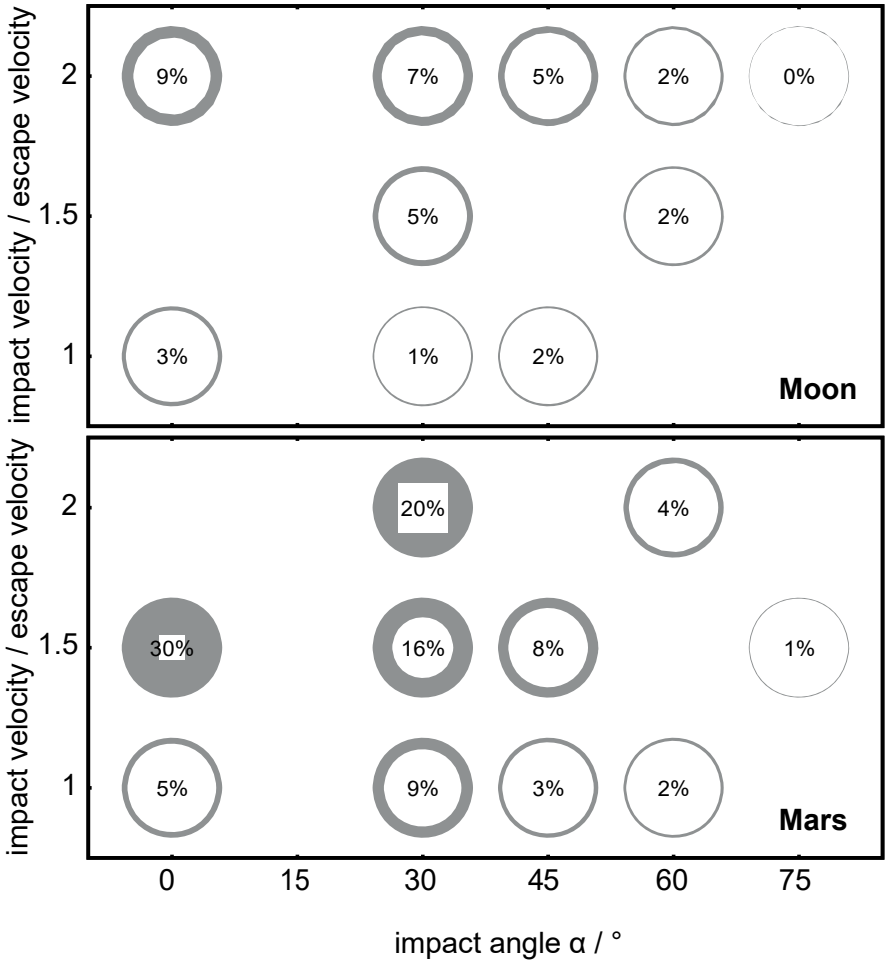

Figure 4: Atmospheric loss scenarios by impacts. Atmosphere losses (in percent) of protoplanets caused by Moon-mass impactors and Mars-sized impactors, as a function of impact angle and impact velocity (in units of v_{esc}).

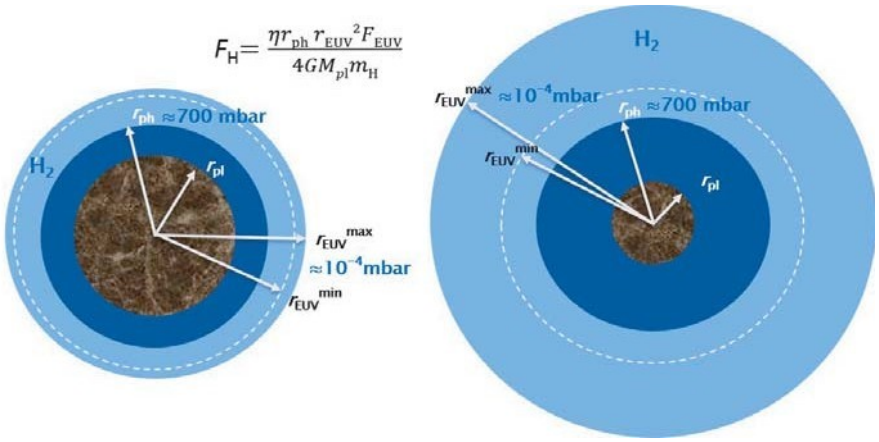

Figure 5: Illustration of the planetary radius r_{pl}, photospheric radius r_{ph} and effective EUV absorption radius r_{EUV} for a massive and less massive planetary body. The dashed white line illustrates r_{EUV} as obtained by the simplified approximations of Watson et al. (1981), which underestimates the energy-limited escape flux F_H from low mass bodies to a great extent compared to the r_{EUV} as obtained by hydrodynamic upper atmosphere structure modeling (Erkaev et al., 2014, 2015).

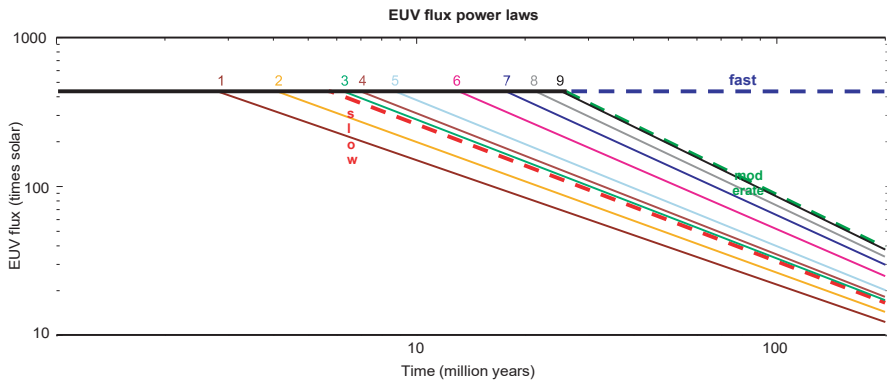

Figure 6: Various EUV flux power laws according to slow, moderate and fast rotating young Sun-like G-stars as a function of time normalized to the present average solar EUV flux.

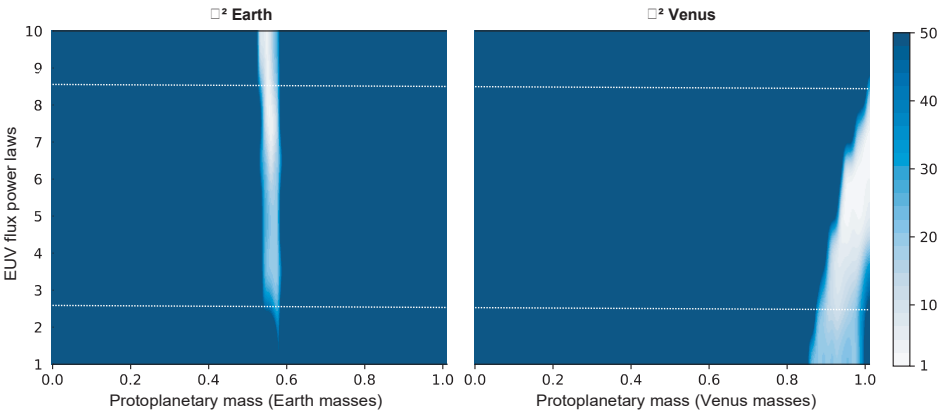

Figure 7: Statistical χ^2 parameter study of the element and isotope evolution for Earth (left panel) and Venus (right panel). This includes the variation of possible initial H_2O and CO_2 atmospheric partial pressures (H_2O/CO_2=5/1, 15/3, 30/6, 75/15), and different nebula life times (3-5 Myr). The observed elemental ratios of both planets can be reproduced if the young Sun was between a slow and a moderate rotating young G-type star with masses of 0.85-1.0 M_{Venus} (0.69-0.81M_{Earth}) and 0.53-0.58 M_{Earth} when the solar nebula disappeared. The horizontal white dotted lines show the range of the EUV flux **(EUV power laws 3 to <9)** in which both planets can be reproduced simultaneously.

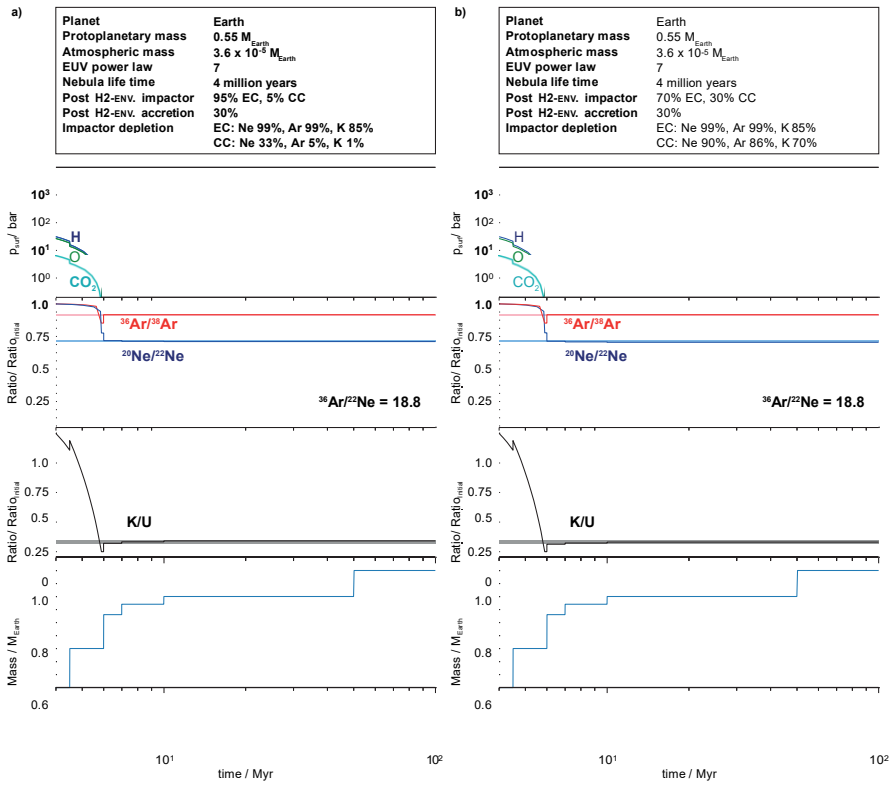

Figure 8: **a) Successful reproduction of Earth's present atmospheric $^{36}Ar/^{38}Ar$, $^{20}Ne/^{22}Ne$, $^{36}Ar/^{22}Ne$ isotope and the BSE K/U ratios of Earth by assuming a composition for Earth's building blocks as inferred by Dauphas (2017) from the analysis of isotopic data from lithophile-siderophile elements. A fast accretion (30% accreted after the H_2-envelope was lost) and 95% strongly depleted (Ar by 99%, Ne by 99% and K by 85%) EC-like material of the post-H_2-envelope impactors with an addition of 5% weakly depleted (Ar by 5%, Ne by 33% and K by 1%) CC are necessary. The EUV activity of the young Sun followed the evolution track given in EUV power law 7. b) The same as a) but with a post-H_2-envelope impactor composition of 70% EC and 30% CC-like material. Here these impactors are also strong depleted in Ar, Ne and elements like K (Ar by 86%, Ne by 90% and K by 70%).**

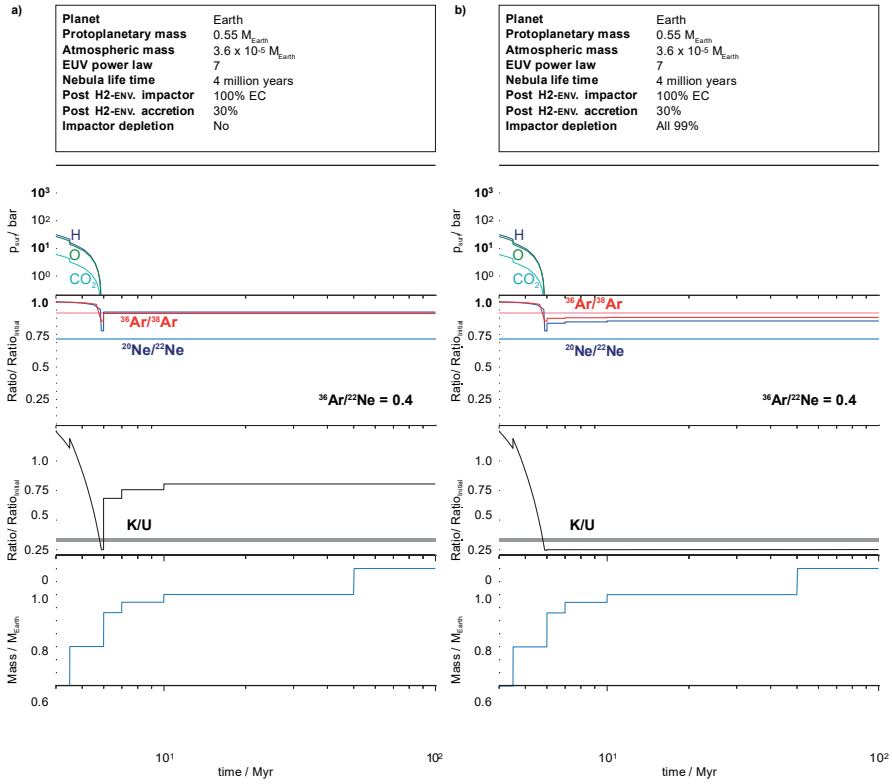

Figure 9: **a) Reproduction attempt of today's atmospheric $^{36}Ar/^{38}Ar$, $^{20}Ne/^{22}Ne$, $^{36}Ar/^{22}Ne$ isotope ratios and the BSE K/U ratios of Earth by assuming a composition for Earth's building blocks as inferred by Dauphas (2017) and similar proto-Earth and young Sun parameters as in Fig. 8a, but with an undepleted 100% post-H_2-envelope impactor EC-like composition. b) The same as a) but the post-H_2-envelope impactors are strongly depleted in Ar, Ne and K (Ar by 99%, Ne by 99% and K by 99%). Here in both cases Earth's present atmospheric $^{20}Ne/^{22}Ne$, $^{36}Ar/^{22}Ne$ isotope ratios and the BSE K/U ratios can not be reproduced.**

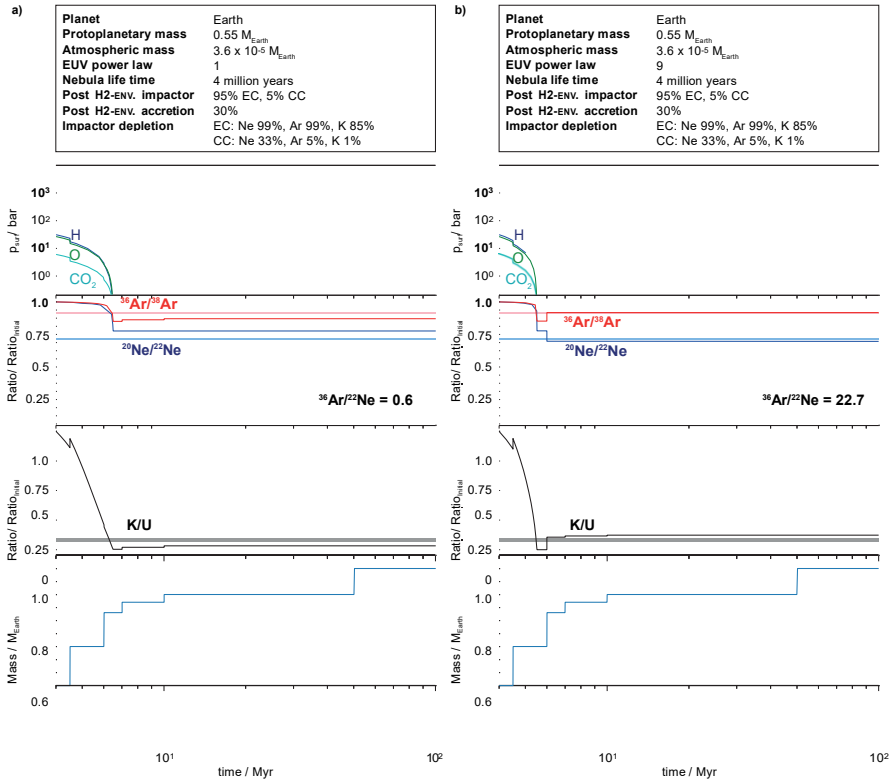

Figure 10: **a) Reproduction attempt of today's atmospheric $^{36}Ar/^{38}Ar$, $^{20}Ne/^{22}Ne$, $^{36}Ar/^{22}Ne$ isotope and the BSE K/U ratios of Earth by assuming a composition for Earth's building blocks as inferred by Dauphas (2017) and Fig. 8a, but exposed to a very weakly rotating young Sun (Fig. 6: EUV power law 1). b) The same as a) but exposed to a moderately rotating young Sun (Fig. 6: EUV power law 9.). Here in both cases Earth's present atmospheric $^{20}Ne/^{22}Ne$, $^{36}Ar/^{22}Ne$ isotope ratios and the BSE K/U ratios can not be reproduced. However, the case shown in panel b) yield a better result compared to the case shown in panel a) with an $^{36}Ar/^{22}Ne$ isotope ratio which results in 22.3 instead of 18.8.**

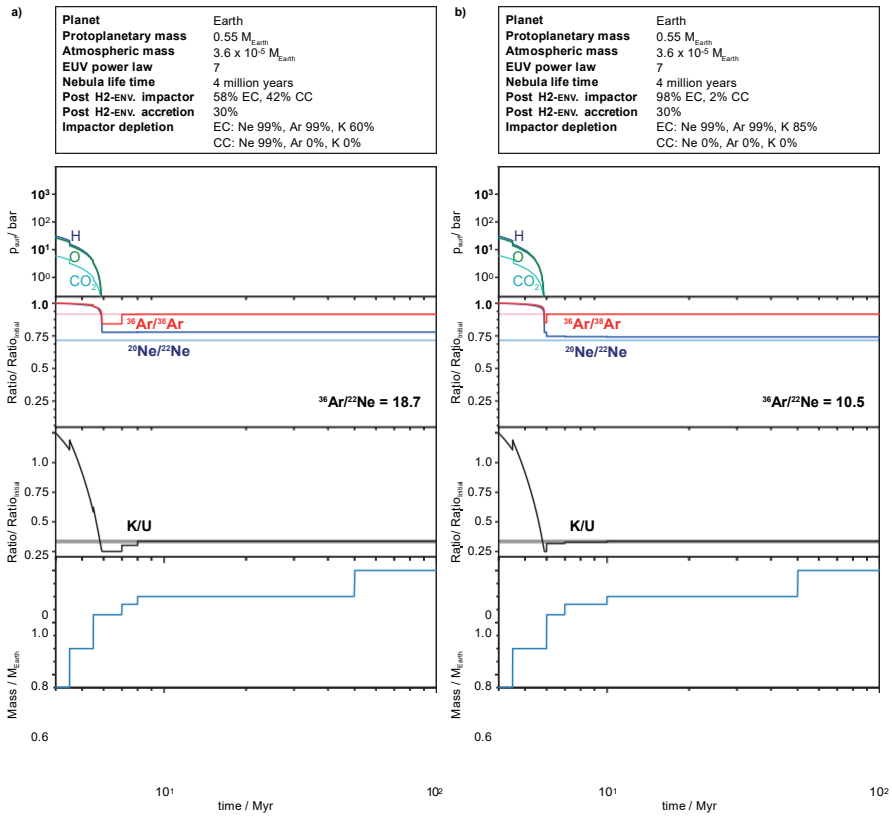

Figure 11: **a) Reproduction attempt of present Earth's atmospheric $^{36}Ar/^{22}Ne$ isotope ratio by assuming arbitrary values for atmospheric $^{36}Ar/^{38}Ar$, $^{20}Ne/^{22}Ne$ isotope and the BSE K/U ratios (Fig. 6: EUV power law 7.). Here the post-H_2-envelope impactor material has a composition of 58% strongly depleted (Ar by 99%, Ne by 99% and K by 99%) EC-like and 42% CC-like materials where Ar and K is not depleted but Ne is depleted by 99%. Although, the $^{20}Ne/^{22}Ne$ isotope ratios can not be reproduced, the $^{36}Ar/^{22}Ne$ isotope ratio yields 17.8, which lies near the present Earth atmospheric ratio it is impossible that CCs are delivered where volatile elements like Ar and K are not depleted but Ne is nearly absent. b) The same parameters as in the case shown in Fig. 8a but with a composition as that discussed in (Marty, 2012) of strongly depleted 98% EC and 2% un-depleted CC-like material. Although, the $^{36}Ar/^{38}Ar$, $^{20}Ne/^{22}Ne$ isotope and the BSE K/U ratios can be roughly reproduced, the atmospheric $^{36}Ar/^{22}Ne$ isotope ratio yields a value of 10.5, which is too low.**

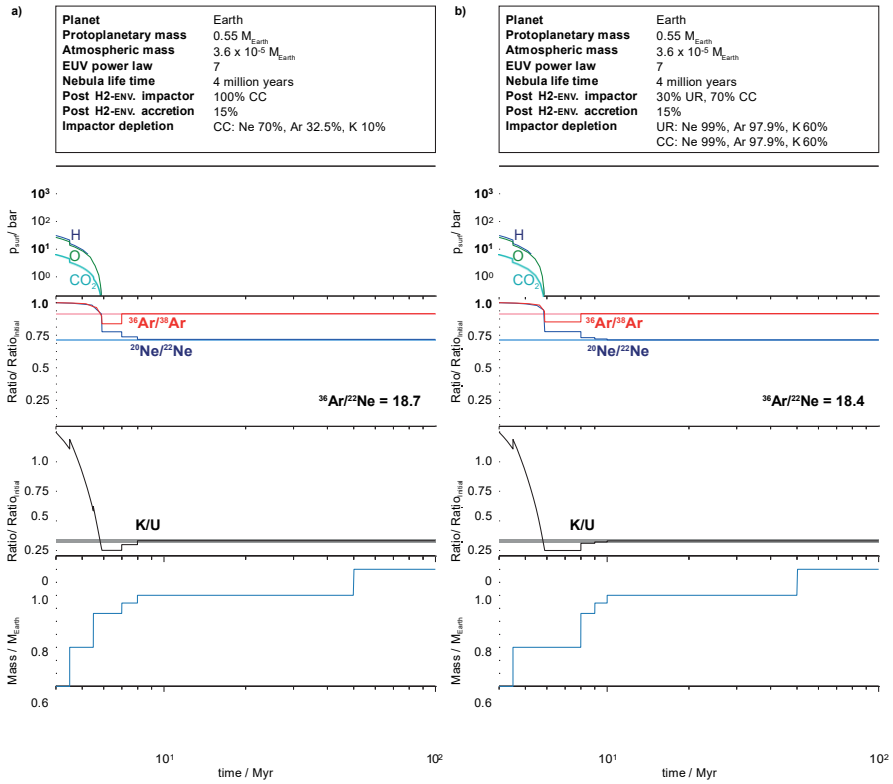

Figure 12: **a) Successful reproduction of Earth's present atmospheric $^{36}Ar/^{38}Ar$, $^{20}Ne/^{22}Ne$, $^{36}Ar/^{22}Ne$ isotope and the BSE K/U ratios of Earth by assuming a composition for Earth's building blocks as inferred by Schiller et al. (2018) from the analysis of Ca-isotopic data. A faster accretion than in the cases related to the building block composition obtained by (Dauphas, 2017) (15-20% accreted after the H_2-envelope was lost) and 100% depleted (Ar by 33%, Ne by 70% and K by 10%) CC-like (or CI-like) material of the post-H_2-envelope impactors are necessary. The EUV activity of the young Sun followed the same evolution track as in the case shown in Fig. 8a (EUV power law 7). b) The same as a) but with a post-H_2-envelope impactor composition of 30% UR and 70% CC-like material. Here these impactors are depleted in Ar by 98%, Ne by 99% and K by 60%.**

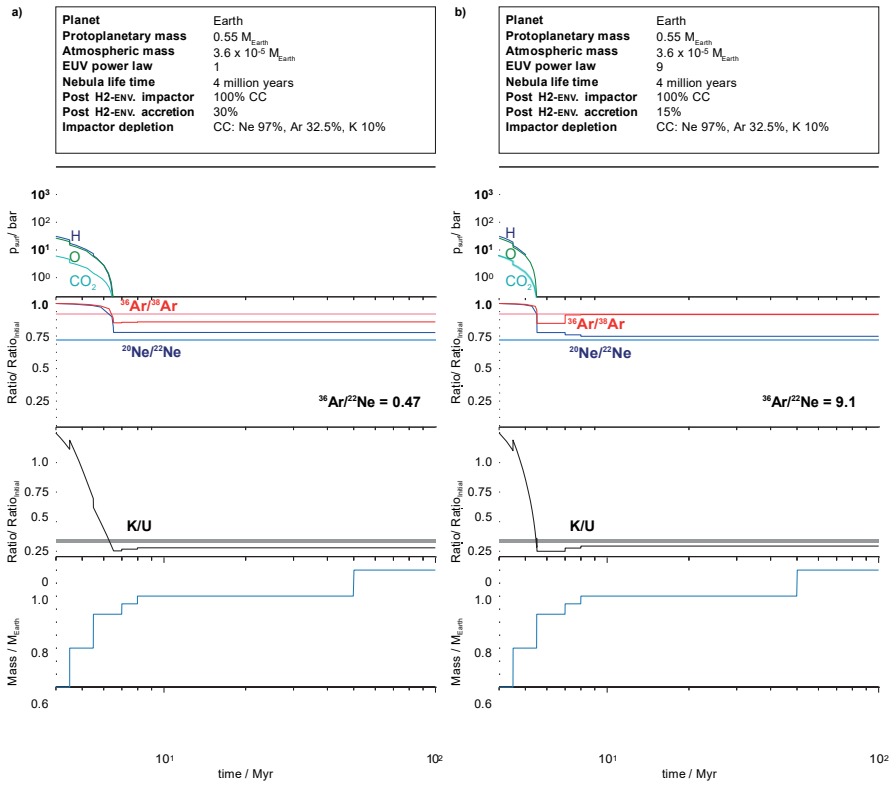

Figure 13: **a) Reproduction attempt of today's atmospheric $^{36}Ar/^{38}Ar$, $^{20}Ne/^{22}Ne$, $^{36}Ar/^{22}Ne$ isotope and the BSE K/U ratios of Earth by assuming a composition for Earth's building blocks as inferred by Schiller et al. (2018) and Fig. 12a, but exposed to a very weakly rotating young Sun (Fig. 6: EUV power law 1.). b) The same as a) but exposed to a moderately rotating young Sun (Fig. 6: EUV power law 9.). Here in both cases Earth's present atmospheric $^{20}Ne/^{22}Ne$, $^{36}Ar/^{22}Ne$ isotope ratios and the BSE K/U ratios can not be reproduced. In both cases the moderately volatile element K is more depleted than the more volatile like Ar which has more or less a similar mass. This is most likely not realistic because very volatile noble gases should be more depleted than elements like K.**

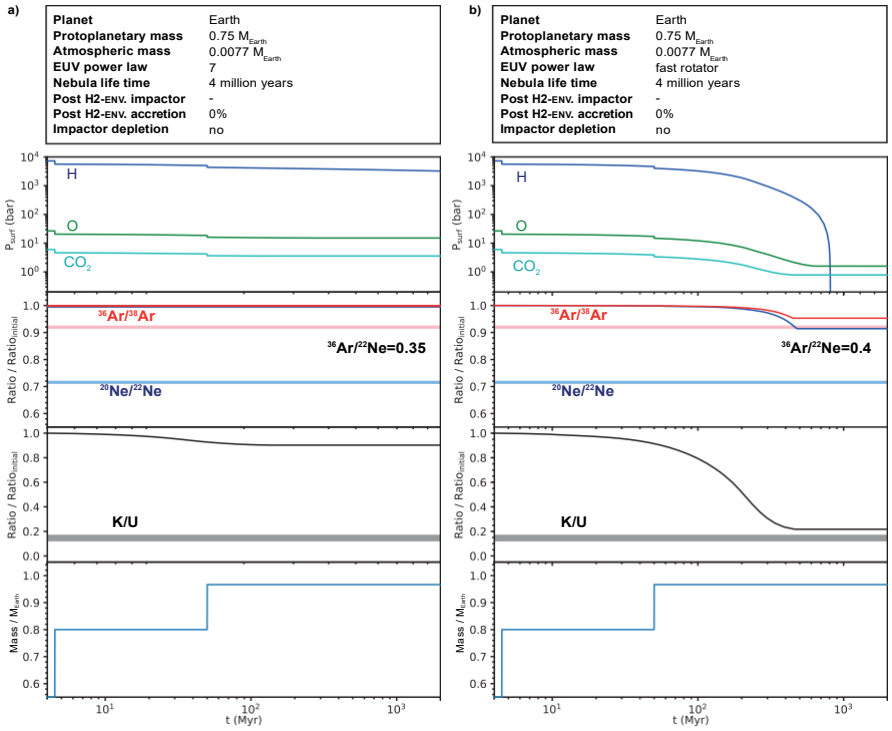

Figure 14: a) Unsuccessful reproduction of today's atmospheric $^{36}/^{38}$Ar, $^{20}/^{22}$Ne and BSE K/U ratios with a proto-Earth mass of $0.75M_{\text{Earth}}$ at 4 Myr that is exposed to the EUV flux of a nearly moderate rotating early Sun. b) Unsuccessful reproduction with a proto-Earth mass of $0.75M_{\text{Earth}}$ at 4 Myr exposed to the EUV flux of an active fast rotating early Sun.

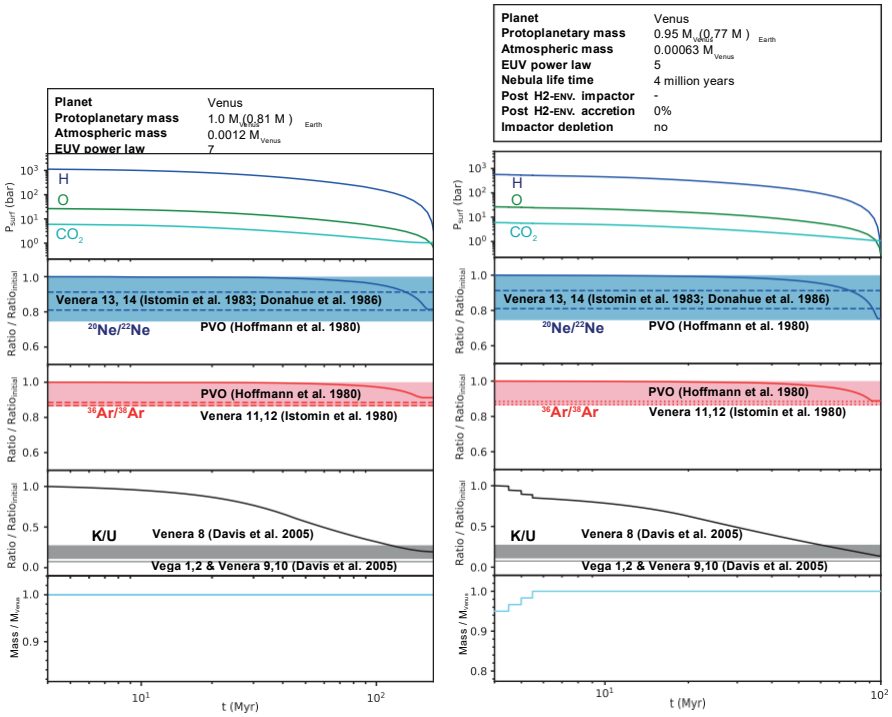

Figure 15: a) Successful reproduction attempt that reproduce the Venera 11 & 12 Ar and Venera 13 & 14 Ne noble gas isotope and K/U ratios within the measured error bars at the Venera 8 landing site. b) Successful reproduction attempt that reproduce Venus' atmospheric Ar noble gas isotope ratio measured by Venera 11 and 12 mass spectrometer data (Istomin et al., 1980) and the K/U ratios within the tiny measured error bars at the Vega 1, 2 and Venera 9 and 10 landing sites (Davis et al., 2005).

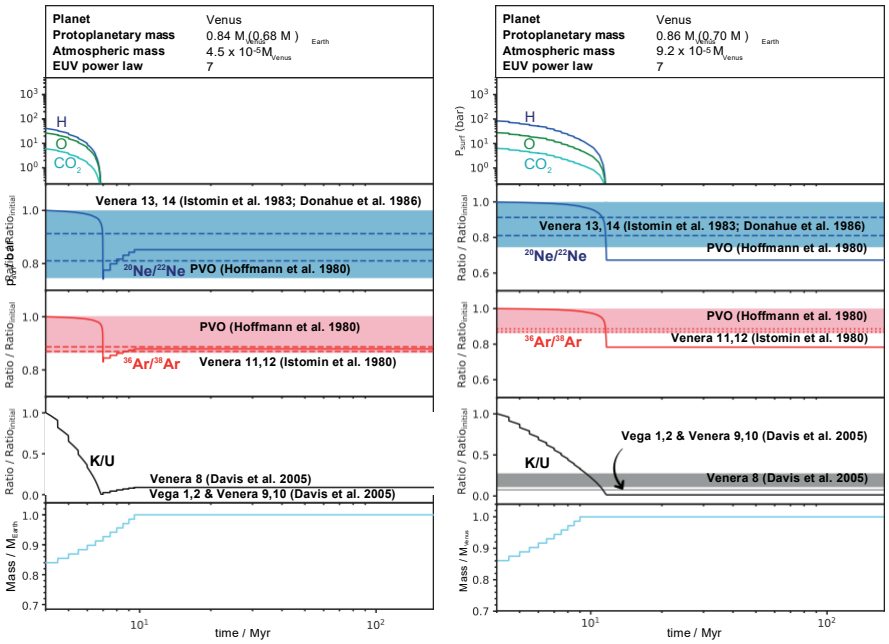

Figure 16: **a) Successful reproduction attempt that reproduce the Venera 11 & 12 Ar and Venera 13 & 14 Ne noble gas isotope and K/U ratios within the measured error bars at the Venera 8 landing site for a low mass Venus of 0.84$M_{\rm Venus}$ with a 100% EC-like building block composition that accreted about 17% of its mass after a small primordial atmosphere was lost at 7 Myr after the origin of the Solar System and 3 Myr after the disk evaporated. Here the post-H_2-envelope impactor EC-like material is depleted in Ar and Ne by 92% and K by 89%.** b) Failed reproduction attempt of the Venus' atmospheric Ar and Ne noble gas isotope ratios. Here, proto-Venus has a mass of 0.86$M_{\rm Venus}$ after dissipation of the circumstellar gas disk at 4 Myr. It captures a small H_2-envelope with a partial surface pressure of 100 bar. The nebula lifetime is assumed to be 4 Myr and the EUV activity of the early Sun is slightly less active than a moderate rotator. Venus' Ne and Ar isotope ratios are over-fractionated with their ratios being outside of the huge error bars as measured by PVO. Interestingly, K/U rock measurements by Vega 1, 2 and Venera 9, 10 at Venus' surface can nevertheless be reproduced in this scenario.

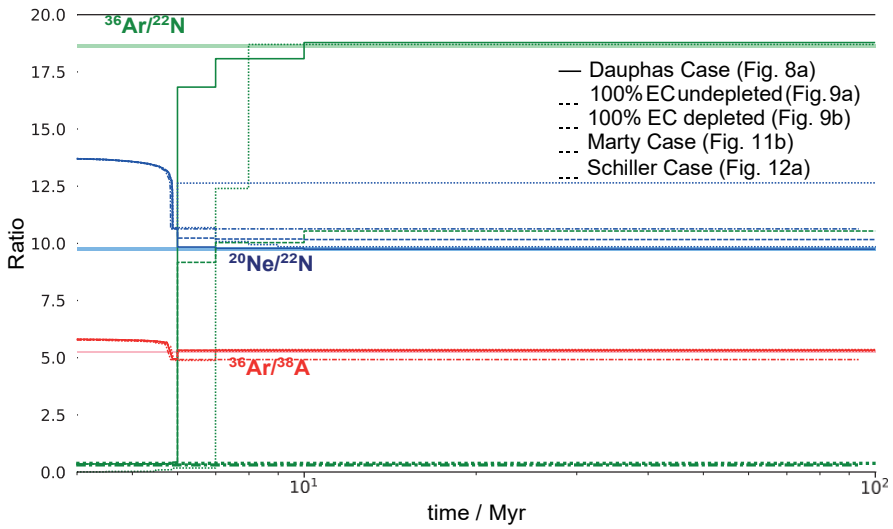

Figure 17: **Evolution of the atmospheric ^{36}Ar/^{22}Ne together with ^{20}Ne/^{22}Ne and ^{36}Ar/^{38}Ar for our cases Fig. 8a, Fig. 9a, Fig. 9b, Fig. 11b and Fig 12a. Of those five cases only the Dauphas and Schiller cases, i.e. the ones with 95% strongly depleted EC and 5% weakly depleted CC-like post H_2-envelope impactor material, and depleted 100% CC-like post H_2-envelope impactors, respectively, can reproduce the present-day atmospheric value of ^{36}Ar/^{22}Ne.**

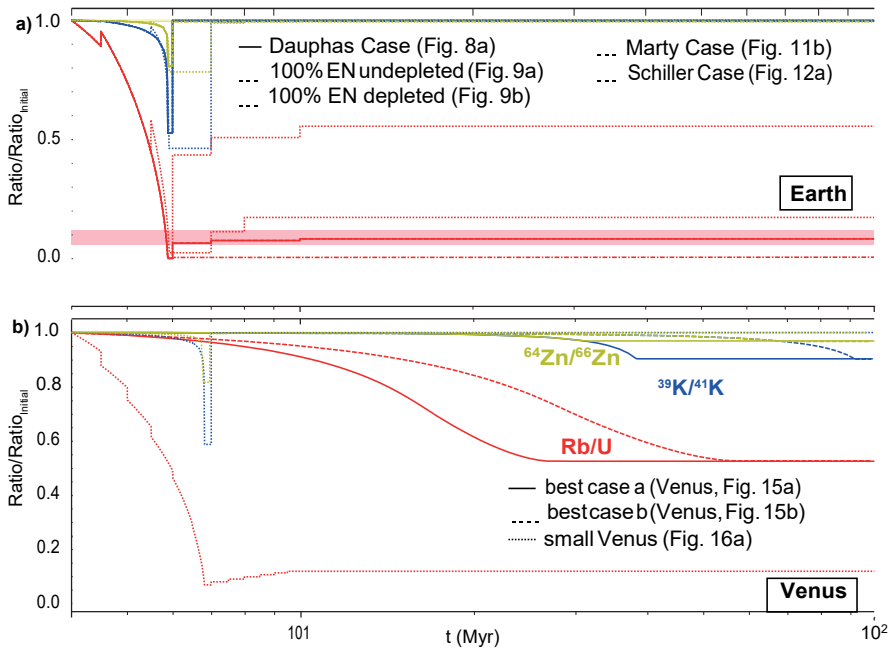

Figure 18: **a) Evolution of ^{66}Zn/^{68}Zn, ^{41}K/^{39}K, and of Rb/U for our cases shown in Fig. 8a, Fig. 9a, Fig. 9b, Fig. 11b and Fig 12a. b) Same, but for the two best Venus case and the small Venus case examples (Fig. 15a, Fig. 15b and Fig. 16a).**

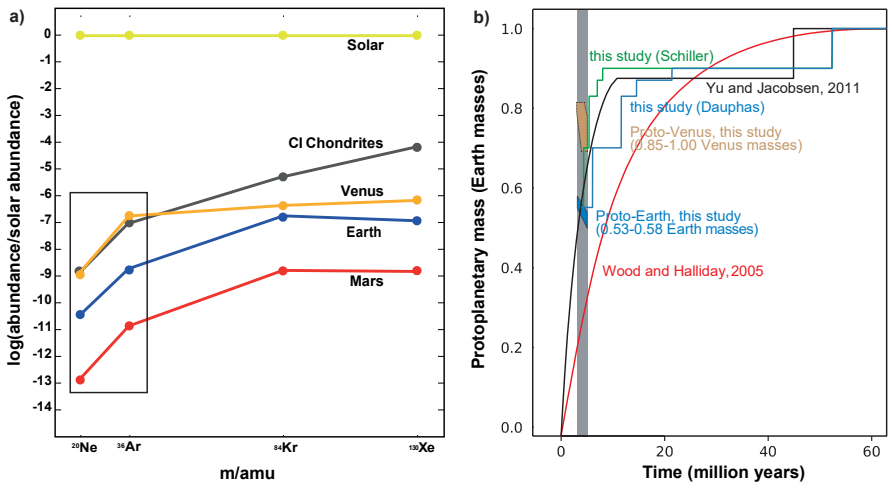

Figure 19: a) Noble gas abundances of Venus, Earth, Mars, and CCs relative to the solar value. Venus has significantly higher abundances of Ar and Ne compared to the Earth and Mars which indicates that Venus lost a smaller amount of these noble gases. A reason for this might be that proto-Venus had a higher mass compared to proto-Earth after the disk dispersal which would be in agreement with our study. b) Accretion scenarios according to ^{182}Hf-^{182}W chronometry of terrestrial rocks after Wood and Halliday (2005) and Yu and Jacobsen (2011) as a function of time compared to the protoplanetary masses of early Venus and Earth of this study for 3-5 Myr. **The Schiller and Dauphas cases are both in good agreement with Yu and Jacobsen (2011), i.e. with ^{182}Hf-^{182}W 5, for a proto-Earth with about 0.55M_{Earth} after 4 Myr**. It has to be noted that the ^{182}Hf-^{182}W data is valid only for the Earth, whereas there is no data for Venus.

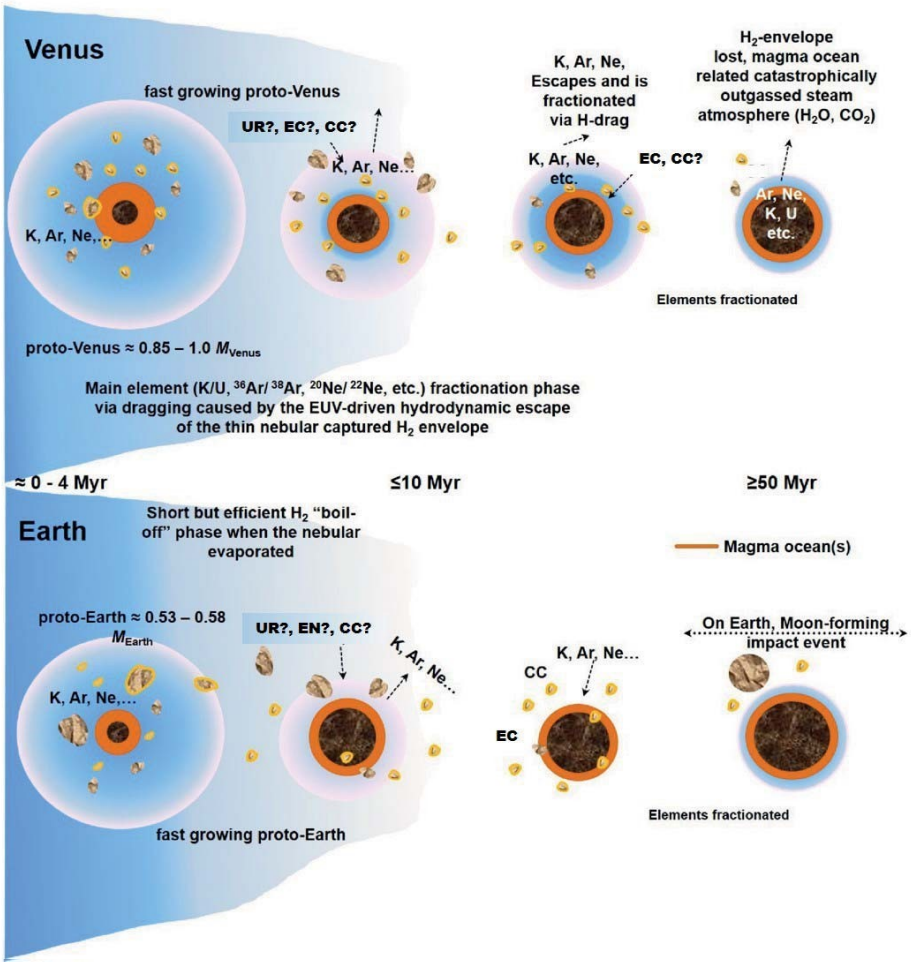

Figure 20: Illustration of most likely evolution scenarios for early Venus and Earth **if both protoplanets captured a small primordial atmosphere** in agreement with today's observed $^{36}Ar/^{38}Ar$, $^{20}Ne/^{22}Ne$ isotope and K/U elemental ratios. Proto-planetary cores accreted fast, while they were embedded in the gas disk (shaded blue area), thus accumulating hydrogen from the solar nebula. After the disappearance of the circumsolar disk, this H_2-envelope is then partly lost during the short but efficient "boil-off" phase and later on completely removed via EUV-driven hydrodynamic escape and giant impacts. During this stage elements with initially solar abundances are fractionated and in addition mixed with the impacting material until accretion is finally finished.